Cell Biol Toxicol (2025) 41:89
https://doi.org/10.1007/s10565-025-10032-8

RESEARCH

IFI204 in microglia mediates traumatic brain injury-induced mitochondrial dysfunction and pyroptosis via SENP7 interaction

Ting Guo · Yongxing Lai · Shuguang Wu · Chunjin Lin · Xinyu Zhou · Peiqiang Lin · Mouwei Zheng · Jianhao Chen · Fan Lin

Received: 24 December 2024 / Accepted: 24 April 2025

Abstract

Objectives Traumatic brain injury (TBI) is a primary contributor to chronic functional impairment in human populations, initiating complex neuroinflammatory cascades and neurodegeneration. Despite extensive research efforts, the precise pathophysiological pathways remain incompletely characterized. This investigation aims to establish a novel therapeutic strategy that targets critical molecular pathways post-injury, potentially addressing the current limitations in the clinical management of TBI patients.

Methods The single-cell data of cortical tissue from mice with TBI were obtained from public databases (GSE160763), which was utilized to identify alterations in in the composition of disease-associated cells and related molecules as the disease progresses. Functional and pathway enrichment analyses were conducted to elucidate the functional characteristics of microglia and astrocyte subpopulations. Trajectory analysis was employed to investigate cell differentiation characteristics. Subsequently, we examined the expression and function of microglia-specific molecules, such as IFI204, along with their underlying molecular mechanisms using Western blotting,

Ting Guo, Yongxing Lai and Shuguang Wu contributed equally to this work.

Supplementary Information The online version contains supplementary material available at https://doi.org/10.1007/s10565-025-10032-8.

T. Guo
Department of Geriatric Medicine, Shanghai Sixth People's Hospital, Affiliated to Shanghai Jiao Tong University School of Medicine, Shanghai, China

Y. Lai · C. Lin · M. Zheng · F. Lin (✉)
Department of Geriatric Medicine, Shengli Clinical Medical College of Fujian Medical University, Fuzhou University Affiliated Provincial Hospital, Fuzhou, China
e-mail: linfan@fjmu.edu.cn

Y. Lai · C. Lin · M. Zheng · F. Lin
Fujian Provincial Center for Geriatrics, Fuzhou, China

S. Wu
Department of Anesthesiology, The Second Affiliated Hospital Zhejiang University School of Medicine, Hangzhou, China

X. Zhou
Department of Neurology, The First Affiliated Hospital of Kangda College of Nanjing Medical University, Lianyungang, China

P. Lin
Department of Neurology, Shengli Clinical Medical College of Fujian Medical University, Fuzhou University Affiliated Provincial Hospital, Fuzhou, China

J. Chen (✉)
Department of Rehabilitation Medicine, Shengli Clinical Medical College of Fujian Medical University, Fuzhou University Affiliated Provincial Hospital, Fuzhou, China
e-mail: lycjh0469@126.com

Published online: 23 May 2025

immunofluorescence, co-immunoprecipitation (CO-IP), histopathology, behavioral tests, and molecular docking to assess binding status, as well as molecular dynamics simulations. Finally, we used molecular docking technology to find small molecule compounds that IFI204 can stably bind to.

Results We identified nine major cell populations, most of which undergo dynamic changes following TBI. Astrocytes and microglia were the predominant populations in each group, and further cluster analysis revealed that the proportions of interferon (IFN) and axonogenesis-related microglial subtypes increased after TBI. Trajectory inference analysis indicated that the expression of Ifi204 is upregulated in microglia during disease progression. Conditional microglial knockdown of IFI204 significantly improved neurological deficits in mice, and alleviated mitochondrial dysfunction and microglial pyroptosis. Mechanistically, SENP7, identified as a novel molecule, interacts with IFI204 in microglia, catalyzes the deSUMOylation of IFI204, and promotes STING signal activation, ultimately driving microglial pyroptosis and mitochondrial dysfunction.

Conclusions The interaction between IFI204 and SENP7 promotes microglial pyroptosis and related mitochondrial dysfunction. Furthermore, in the case of TBI, we hypothesize that targeting IFI204 might yield therapeutic benefits.

Keywords IFI204 · SENP7 · Mitochondria · Microglial pyroptosis · Traumatic brain injury

Introduction

Concerning the elderly, Traumatic brain injury (TBI) is one of the most notable contributors to the mortality rate, as well as death due to neurodegenerative diseases, and mental illnesses (Khellaf et al. 2019). Nearly 69 million individuals are affected by TBI annually (Dewan 2018). There is a lack of adequate and proper treatment methodologies for TBI. Therefore, thorough comprehension of the molecular pathways altered in TBI is essential for developing targeted therapies. Emerging research has identified multiple molecular indicators linked to TBI pathogenesis. Nevertheless, current findings derived from isolated datasets or limited cohort sizes present methodological constraints that compromise their reliability. This underscores the critical need for systematic validation through large-scale multicenter studies. Consequently, precise molecular characterization of TBI-associated signatures remains imperative for advancing diagnostic precision and therapeutic development in clinical neurology.

One way to study how cells respond to injury is through transcriptome analysis of the different cell types present at the injury site. However, previous studies have been limited to focusing on only one type of cell, lacking information on the diversity of subpopulations and various cellular conditions. The more recent advances in single-cell RNA sequencing (scRNA-seq) technology has now accurately represent particular distinct subpopulations within a particular cell type, which overcomes the prior limitations (Heiman 2008;, Sanz et al. 2009). Furthermore, it is now possible to obtain and analyze multiple cell types from one tissue sample which enables the study of the relationships and the means of communication among different cells. In one of my prior studies, we focused on the analysis of 13,471 cells from the control group and 9,482 cells from the test group (TBI). All the data we generated using the numerous advanced analytical techniques at our disposal strongly suggest that there are multiple states of microglial cells present as we move towards Day 7 post TBI, indicating a temporal shift towards a more non-steady condition. In addition, Ifi204 may be associated with disease progression and poor prognosis in mice after TBI, and is anticipated to emerge as a potential therapeutic target for precision medicine in the future.

Post-traumatic neuroinflammatory processes within the compromised cerebral tissue constitute a critical component of secondary injury mechanisms following TBI, primarily marked by the activation of microglia (Wang et al. 2014). Moreover, excessive or prolonged neuroinflammation can result in neurological deficits following TBI (Song 2022). Pyroptosis, is mediated through inflammasome activation and subsequent gasdermin D (GSDMD) cleavage. The proteolytically liberated amino-terminal fragment (GSDMD-NT) induces transmembrane pore formation, facilitating extracellular release of inflammatory mediators, thereby amplifying inflammatory signaling cascades (Xu 2019). Experimental evidence from both in vitro microglial models and murine traumatic brain injury studies confirms the operational

involvement of the NOD-like receptor thermal protein domain associated protein 3(NLRP3)/Caspase-1/GSDMD axis in neuroinflammatory responses. This molecular pathway demonstrates particular significance in modulating post-traumatic glial activation dynamics and associated neuropathological sequelae (Li 2024). These studies indicate targeted strategies to restrain microglial pyroptosis may be of significant therapeutic importance.

After TBI, a variety of post-injury cascades are triggered, which encompass mechanisms such as apoptosis, pyroptosis, inflammation, and oxidative stress. These processes can lead to systemic effects that exacerbate the overall impact of TBI (Xu 2023). Recent research indicates that elevated oxidative stress, resulting from overly activated microglia, promoting neuronal apoptosis and exacerbating brain injury after TBI (Juárez-Rebollar et al. 2017;, Su 2021). The overproduction of ROS, along with the reduced activity of antioxidant enzymes like GSH-Px, has been noted during oxidative stress episodes, which in turn exacerbates the oxidative stress (Guo 2023;, Liu 2018). Therefore, developing novel compounds to mitigate mitochondria oxidative stress may help ameliorate neuronal death and aid in the treatment of TBI.

stimulator of interferon genes (STING) specifically activates innate immunity signaling pathways, initiating a response characterized by type I interferon (Zhou et al. 2022). Research indicates that inhibiting STING can alleviate neuroinflammation and reduce neuronal apoptosis in mice suffering from TBI (Shi 2023). Furthermore, STING is implicated in eliciting various stress responses in vascular smooth muscle cells (VSMCs), which contribute to aortic degeneration and aneurysm formation (Luo 2020). Additional studies have shown that the upregulation of STING can lead to neuroinflammation, synaptic deterioration, and the death of neural cells in vitro under conditions of chronic oxidative stress (Sanders 2023;, Gaidt 2017). While various aspects of STING's impact have been explored, its specific contribution to TBI, along with its potential regulatory impact on microglial pyroptosis and mitochondrial dysfunction, remains unexamined.

Interferon-inducible protein 204 (IFI204) belongs to the p200 family of proteins that are induced by interferon. A previous study has shown that the IfI204, whose gene product, p204, p204 overexpression in Mouse squamous cell carcinoma (SCCVII) cells significantly inhibited cell growth (Yamaguchi et al. 2019). P204 can promote apoptosis of various cell types and inhibit cell viability and migration (Liu 2000). Emerging evidence suggests IFI204 mediates chronic inflammatory processes and autoimmune pathogenesis. This molecular cascade demonstrates how aberrant immune activation may ultimately drive tissue destruction through sustained pro-inflammatory signaling pathways (Mondini et al. 2010;, Choubey 2010). In a spontaneous model of prostate cancer, IFI204 reduces the density of intraductal microvessels and the proliferation of tumor cells (Persano 2009). Although the effects of IFI204 have been discussed, it is still necessary to investigate whether IFI204 serves as a key regulator in mitochondrial dysfunction and cell pyroptosis induced by microglia following TBI.

SUMOylation, a dynamic and reversible enzymatic process governing post-translational protein modifications, entails the site-specific covalent conjugation of small ubiquitin-like modifier (SUMO) proteins of select lysine residues in substrate polypeptides. This molecular mechanism, characterized by its cyclical nature, regulates diverse cellular functions through precise modulation of protein interactions and subcellular localization (Cao et al. 2023). This dynamic process is counterbalanced by specialized cysteine proteases that catalyze SUMO-protein dissociation. Notably, the sentrin-specific protease (SENP) family serves as critical regulators in maintaining cellular homeostasis through precise control of SUMO deconjugation from substrate proteins (Lin 2020). SUMOylation serves as a pivotal modulator of diverse biological pathways by dynamically regulating substrate localization, enzymatic activity, protein–protein interactions, and metabolic stability. This post-translational modification critically influences fundamental cellular mechanisms including transcriptional regulation, chromatin remodeling, ion transport dynamics, and oxidative stress adaptation (Hwang et al. 2022). Among key regulatory enzymes, sentrin-specific protease SUMO1/sentrin/SMT3 specific peptidase 3 (SENP3) demonstrates particular significance in cardiovascular pathophysiology. This protease catalyzes the deconjugation process of SUMO-2/3-modified proteins, with its deSUMOylation activity emerging as a critical determinant in mitigating ischemic myocardial injury at the cellular level (Zhou 2019;, Du 2021). Moreover, SENP3 has been found to promote the

inflammatory response activated by lipopolysaccharide (LPS) in macrophages (Chen et al. 2020;, Lao 2018). It has also been observed that oxidative stress induces the interaction between IFI204 and SENP3, leading to IFI204 deSUMOylation, which subsequently facilitates STING-mediated antitumor activity (Hu 2021). SUMO-specific protease 7 (SENP7), a critical regulator of SUMO2/3 conjugation dynamics, modulates essential biological pathways including epithelial-mesenchymal plasticity, genomic stability maintenance, and innate immunity regulation (Bawa-Khalfe 2012; Garvin 2013; Cui 2017). Experimental evidence demonstrates that SENP7 deficiency significantly attenuates cell pyroptotic. This phenomenon likely stems from dysregulated protein hyperSUMOylation induced by compromised SENP7 activity, which disrupts normal post-translational modification homeostasis (Li et al. 2020). IFI204 has previously been described to regulate by SUMOylation modification (Hu 2021). However, whether SENP7 interacted with IFI204, leading to IFI204 deSUMOylation, affecting microglia-induced mitochondrial dysfunction, cell pyroptosis, and inflammation after TBI, has not previously been defined.

In this study, we conducted a thorough examination of scRNA-seq data derived from an earlier investigation (GSE160763) to capture and study cellular and molecular adaptations associated with TBI at single-cell resolution (Witcher 2021). The pathological role of IFI204 in microglia-induced mitochondrial dysfunction and pyroptosis after TBI was explored. Our results indicate that the interaction between SENP7 and IFI204 leads to deSUMOylation of IFI204. Following STING activation, it leads to mitochondrial dysfunction and microglial pyroptosis after TBI. In contrast, IFI204 knockout effectively improves neurological function after TBI by reducing mitochondrial dysfunction and microglial pyroptosis. This research indicates that therapeutic approaches aimed at modulating IFI204 expression or its interaction with SENP7 have the potential to be used as therapeutic strategies for treating TBI.

Materials and methods

scRNA-seq data preprocessing and analysis

The scRNA-seq dataset for TBI in mice was sourced from GSE160763 (https://www.ncbi.nlm.nih.gov/geo/query/acc.cgi?acc=GSE160763)(Witcher 2021), which contained 2 Control and 2 TBI mice. The raw gene expression matrix was converted into a Seurat object utilizing the Seurat R package. Genes expressed in at least five cells per sample were retained, along with cells that expressed more than 200 genes. To further filter out low-quality cells, we retained only those cells that expressed between 200 and 2000 genes, had lower than 5% mitochondrial reads. Following this, we normalized the data matrix by applying the "NormalizeData" function in Seurat. The logarithmized normalized data matrix was scaled based on the top 3000 most variable genes by using the "FindVariableFeatures" function in Seurat. After preprocessing the data, we reduced its dimensionality through principal component analysis (PCA). Batch correction was performed on various Seurat objects utilizing the "RunHarmony" function found in the harmony package. Data clustering was performed using the graph-based clustering method from the "FindNeighbors" function of the Seurat package based on the top 20 principal components, followed by the "FindClusters" function (resolution = 0.5). Visualization was achieved using the "RunTSNE" function to generate a two-dimensional t-distributed stochastic neighbor embedding (t-SNE) plot with the "dims" parameter set to 1:15. Subsequently, cell clusters were manually categorized into major cell types according to established markers. The COSG package, with default parameters, was utilized to identify marker genes for each cell type. For subclustering of the main cell types (Microglia and Astrocytes), the same procedures for identifying the most variable genes, batch correction, dimensionality reduction, and cell annotation were repeated.

Functional-enrichment analysis

The COSG package was employed to identify markers associated with each cell type in order to investigate their functions. The top 25 genes across different cell types underwent Gene Ontology (GO) functional annotation analysis utilizing the clusterProfiler R package (Yu et al. 2012). Furthermore, Gene Set Enrichment Analysis (GSEA) was conducted to evaluate the status of pathway enrichment based on the differentially expressed genes (DEGs) among subcell types (Subramanian 2005).

Trajectory analysis

The Monocle2 R package was utilized to elucidate the differentiation trajectories of the cell subtypes (Qiu 2017). Briefly, the expression profiles from interesting cell clusters were converted into Monocle CellData-Set using the "newCellDataSet" function of monocle2 (set lowerDetectionLimit = 0.5). The low-quality cells and genes were then removed utilizing the "detectGenes" function with (set min_exp = 0.1). Significant DEGs among subcellular types along pseudotime were identified using the "differentialGeneTest" function (qval < 0.01). The "DDRTree" method from the "reduceDimension" function was employed to reduce the dimensions. The "plot_cell_trajectory", plot_genes_in_pseudotime", and "plot_pseudotime_heatmap2″ functions were applied for visualization after cell ordering.

Animals

The IFI204floxed (IFI204$^{f/f}$) and Cx3cr1^{CreERT2} lines of mice were produced by Shanghai Model Organisms Center in China. To create mice with a specific knockout of microglia, the homozygous IFI204$^{f/f}$ mice were intercrossed with Cx3cr1^{CreERT2} mice which have tamoxifen (TAM) inducible Cre-recombinase under the control of the Cx3cr1 promoter. TAM was administered to the mice through intragastric administration for attaining the desired microglia knockout. Mice were housed in standardized filter-top enclosures under controlled 12-h light/dark cycles.

Tamoxifen administration

TAM (Sigma) citrate was gavaged at 200 μg/g twice a day for three days starting at one month of age (Li 2020). For postnatal mice, 100 μg of corn oil-soluble TAM was injected intraperitoneally on postnatal days 1 and 2, initiating Cre recombination during the two days of injection.

Traumatic brain injury (TBI) model and experimental groups

A TBI model was established in mice using craniotomy and impact, as previously described (Shi 2023). During the surgical procedure, the mice were administered anesthesia using sodium pentobarbital (40 mg/kg, intraperitoneally). The mice was carefully secured in a stereotaxic instrument designed for precise positioning and immobilization of small animals during surgical procedures. Subsequently, a cranial window with a diameter of 3.5 mm was created above the right parietotemporal region of the skull. This specific location was determined to be 2.5 mm posterior to the bregma and 2.5 mm lateral to the sagittal suture. The cranial window was made using a precision motorized drill, ensuring accuracy and minimizing trauma to the surrounding tissues during this delicate procedure. TBI was generated using a flat probe with a diameter of 3 mm, 3.5 m/s impact speed, 200 ms dwelling time, which resulted in an impact depth of 2.2 mm. In contrast, the mice in the sham group experienced identical handling protocols, although craniotomy and impact were not performed. The experimental groups were categorized as follows: the IFI204$^{f/f}$-Sham group, the IFI204 cKO-Sham group, the IFI204$^{f/f}$-TBI group, and the IFI204 cKO-TBI group.

Evaluation of neurological function

Neurological deficiencies were identified before experiencing a TBI, as well as within 24 h, 72 h, and one week after TBI. The evaluation of different groups'sensorimotor abilities was performed through the utilization of modified neurological severity scores (mNSS) (Zhu 2014). The appraisal of neurological deficiencies was carried out by implementing a scoring system that spanned from 0 to 18.

The evaluation of dynamic balance in experimental animals was primarily conducted using the mouse rota-rod 47,600 (Ugo Basile, Milan, Italy) (Fukuoka 2018). To ensure proper preparation for the test, a 3-day training period was dedicated prior to initiating TBI. The equipment parameters were adjusted to gradually increase the rotational speed from 4 rotations per minute to 40 rotations per minute over a duration of 300 s. Three evaluations were performed daily, with a 15-min interval between each session. The recorded measurement was how long the animals held onto the rotating rod. Subsequently, statistical analysis was conducted using the mean values obtained from the test data.

The neuromuscular performance of the animals was examined by conducting a grip strength assessment. The adaptive training was initiated

seventy-two hours before the TBI (Shen 2019). In this assessment, the mice firmly gripped the grip plate of the grip strength tester (Yiyan Technology Development Co Ltd, Shan Dong) with their two front limbs. The highest amount of force needed for the mouse to slip off the plate was recorded by applying backward force on the mouse's tail using the right hand.

In the foot fault assessment, the sensorimotor functions of the forepaw were evaluated using a previously established method, and we have made some changes. To put it simply, Mice were allowed to navigate freely on a metallic grid surface for a duration of 2 min, with a foot fault recorded when a forepaw slipped or fell between the wires. Prior to the surgical procedure, the mice underwent training for three consecutive days, participating in three sessions each day, with each session lasting 2 min. The proportion of contralateral forepaw staggered steps after TBI in mice = the number of contralateral forepaw staggered steps/the total number of steps taken by the contralateral forepaw*100%. The training results from the final day before surgery served as the baseline reference. Assessments were conducted on 1 d, 3 d, and 7 d following the surgery.

Hematoxylin–Eosin (HE) staining

Briefly, a perfusion of 0.1 M PBS was conducted initially, and this was succeed by a perfusion with 4% PFA. Post-extraction, cerebral specimens were immersion-fixed in 4% PFA, followed by sequential dehydration through a graded ethanol series (70% to 100%), xylene-mediated transparency, and paraffin embedding. The desired brain slices were obtained by sectioning the brain tissue with a rotary microtome (Leica, Germany), and these slices were subsequently placed on glass slides. For histological analysis, deparaffinized sections were subjected to hematoxylin staining (1 min), rinsed thrice with deionized water, and differentiated in 1% acid ethanol for 30 s. Counterstaining with eosin (50 s) preceded final dehydration via absolute ethanol. Coverslips were applied using neutral balsam mounting medium. Morphological evaluation was conducted under bright-field microscopy (Olympus, Japan), with digital image acquisition performed at standardized magnifications.

Nissl staining

Initially, a perfusion of 0.1 M PBS was conducted initially, and this was succeed by a perfusion with 4% PFA. The mouse brain tissue from the mice were submerged immersed in 4% PFA and then treated with a gradient series of alcohol, xylene, and other solvents prior to dehydration and wax immersion. Using a microtome (Leica, Germany), the brain tissue from paraffin-embedded mice was cut into transverse slices. The paraffin sections were dewaxed and then subjected to staining using Nissl staining solution (Sodium tetraborate and toluidine blue), incubating the sections at room temperature for 5 min. Following this, they were differentiated with 1% glacial acetic acid for 3 s and subsequently rinsed with distilled water. Subsequently, the sections were cleared and covered. Microscope images were obtained using an Olympus device from Japan.

Primary culture of microglia

Microglia was cultured according to established methods (Gao 2019). Following enzymatic dissociation of cortical tissue, cells were plated in culture vessels and incubated under controlled conditions (37 °C, 5% CO_2, 95% humidity) using growth medium consisting of Minimum Essential Medium (MEM, Fisher Scientific) supplemented with 10% fetal bovine serum (FBS, Fisher Scientific) and 1% antibiotic–antimycotic solution (penicillin–streptomycin, Fisher Scientific). All reagents were sterile-filtered prior to use. Following a culture period of 12–14 days, mature microglia were obtained from mixed glial cultures through a rapid shaking process, then resuspended in MEM with an addition of 3% FBS, and subsequently transferred to plates.

Establishment of a microglia oxygen and glucose deprivation/reoxygenation (OGD/R) model and experimental groups

In brief, the standard culture medium was substituted with DMEM devoid of glucose (Gibco), and cellular injury was induced by incubating the cultures under hypoxic conditions (95% N2 and 5% CO2) for 2 hours (Xia 2021). Post-OGD, cells were replenished with standard culture medium and maintained in a normoxic incubator (5% CO2) for

24 h to allow recovery. The negative control group did not undergo OGD treatment. Cell transfection, along with the application of LV-sh_SENP7 (MOI = 10), was performed following the manufacturer's guidelines (Hanbio). The transfection efficiency was assessed three days after the procedure. For in vitro experiments, microglia cells were pre-incubated with DMXAA. DMXAA at 20 μg/ml 6 h before oxygen–glucose deprivation (OGD) according to a previous study (Kerr et al. 2019;, Downey et al. 2014). The experimental groups were categorized as follows: for the early stage: the IFI204$^{f/f}$-Control, IFI204 cKO-Control, the IFI204$^{f/f}$-OGD/R, and the IFI204 cKO-OGD/R; for the late stage: the IFI204$^{f/f}$-Control, the IFI204$^{f/f}$-OGD/R, the IFI204 cKO-OGD/R, the LV-sh_SENP7-OGD/R, the IFI204 cKO-DMXAA-OGD/R.

Lipid peroxidation and antioxidant measurements and reactive oxygen species activity detection

Malondialdehyde (MDA) concentrations were determined via a Lipid Peroxidation Assay Kit (Beyotime), while Superoxide Dismutase (SOD) enzymatic activity was analyzed using a corresponding SOD Detection Kit (Beyotime). The glutathione redox status, expressed as the GSH/GSSG ratio, was quantified with a dedicated Glutathione Assay Kit (Beyotime). Additionally, Glutathione Peroxidase (GSH-PX) activity was evaluated through a commercially available GSH-PX Activity Assay Kit (Nanjing Jiancheng Bioengineering Institute). Reactive Oxygen Species (ROS) levels in tissue samples were measured utilizing a Tissue ROS Detection Kit (Biolab).

ROS detection assay

Intracellular ROS were quantified employing a commercial detection kit (Beyotime). For ROS generation study, different groups cells were incubated with 2′,7′-dichlorodihydrofluorescein diacetate (DCFH-DA, 10 μM) in fresh medium at 37 °C for 20 min. The nucleus and mitochondria were stained with 6-diamin-2-phenylindole-dihydrochloride (DAPI). Observations of the images were conducted with a confocal microscope (LSM 750, Zeiss, Göttingen).

Mitochondrial staining

MitoTracker Red CMXRos (Invitrogen) was employed to evaluate mitochondrial structure according to the manufacturer's guidelines. In summary, primary microglia that were plated on coverslips underwent washing with pre-heated PBS. The nucleus and mitochondria were stained with DAPI and a concentration of 100 nM MitoTracker Red CMXRos, respectively. Subsequently, the cells were preserved using formalin to facilitate morphological visualization. Observations of the images were conducted with a confocal microscope (LSM 750, Zeiss, Göttingen).

Mitochondrial membrane potential measurement (ΔΨm)

The assessment of the ΔΨm was performed using a JC-1 kit (Beyotime). In summary, primary microglia were grown in 25 cm^2 flasks (with a density of 3×10^6 cells/flask), followed by centrifugation. The resulting pellet was then incubated in the dark with 2 mL of the prepared solution. This was followed by another centrifugation step. After washing with the buffer solution, samples were analyzed using a BD LSRFortessa (BD Biosciences, CA). Data processing was performed using FlowJo 10.8.1 (BD Biosciences, CA), and results are presented in terms of red fluorescence/green fluorescence ratio.

Western blot

Briefly, protein was applied to electrophoresis, electroporation, blocking, and incubation with the primary antibodies: IFI204 (Abcam), GSDMD (Abcam), GSDMD-N (Cell Signaling Technology, CST), Pro caspase-1 (Adipogen), caspase-1 p20 (Cell Signaling Technology), SENP7 (Santa Cruz Biotechnologies), SUMO2/3 (Proteintech), TBK1 (Cell Signaling Technology), phospho-TBK1 (CST), p-STING (CST), STING (CST), β-actin (Immunoway). After performing three washes, HRP-conjugated goat antibodies that are specific to rabbit or mouse IgG (both sourced from Millipore) were applied at room temperature for a duration of 60 min. Post incubation, visual imaging of the bands was done using a FluorChem M system (ProteinSimple, San Jose).

Immunofluorescence staining

To perform immunofluorescence staining, the slices were first treated with glycine. Then, a blocking solution was applied to the slices. Next, the tissue slices were treated overnight with primary antibodies. The antibodies employed were Iba-1 (Servicebio) and GSDMD (Proteintech). Following this procedure, the slices underwent three washes. The slices were incubated with the secondary antibodies: CoraLite488-conjugated Goat Anti-Rabbit (Proteintech) and Alexa Fluor 594 Goat Anti-mouse (Abcam). Following three more washes, nuclear staining of brain slices was performed using DAPI (Servicebio). After conducting three more washes, the slides were examined with a confocal microscope (LSM 750, Zeiss). The immunofluorescence values were determined through the use of Image-Pro Plus 6.0.

Real-time quantitative PCR (qRT-PCR)

qRT-PCR was conducted with a kit from Yeasen (Shanghai). qRT-PCR was performed with the Applied Biosystems 7500 Real-time PCR System, utilizing SYBR Green Master Mix (Yeasen). β-actin was employed as the internal control in this analysis. The primers used for RT-PCR were summarized in Table S1. The relative mRNA expression of IL-1β, IL-18 was measured using the $2^{-\Delta\Delta CT}$ method and normalized against the mRNA levels of β-actin.

Co-immunoprecipitation assay (Co-IP)

Co-immunoprecipitation experiments were performed by homogenizing cellular material in IP lysis buffer containing protease inhibitors (Progena, Madison), phosphatase inhibitors (Roche), and 5 mM N-ethylmaleimide (Sigma). Lysates were subjected to immunoprecipitation with target-specific antibodies under gentle rotation. Protein-A/G agarose beads (Calbiochem) were subsequently added and incubated with the complexes at 4 °C for 4 h. After sequential washing and elution steps, the immunoprecipitated proteins were resuspended in Laemmli buffer and resolved by SDS-PAGE for immunoblotting. Primary antibodies targeting IFI204 (Abcam), SENP7 (Santa Cruz Biotechnology), and SUMO2/3 (Santa Cruz Biotechnology) were employed for antigen detection.

Molecular dynamics (MD) trajectories analysis and molecular docking

The molecular system, comprising a sodium ion (Na +) equilibrium configuration and a solvation box, employed the TIP3P water model for solvation representation. Long-range electrostatic forces were calculated through the particle mesh Ewald (PME) approach. Simulations implemented Verlet and conjugate gradient (CG) algorithms with a 1.2 nm cutoff distance, while non-bonded interactions were evaluated within a 10 Å range. Energy minimization was achieved via the steepest descent algorithm, capped at 50,000 optimization cycles. Van der Waals and Coulombic interaction thresholds were set at 1.4 nm. System equilibration sequentially employed NVT (constant particle number, volume, and temperature) and NPT (constant particle number, pressure, and temperature) ensembles. Independent 200-ns MD simulations were executed for IFI204 and SENP7 systems. Hydrogen-bond constraints were implemented through the LINCS protocol with 2-femtosecond time steps. Thermal regulation at 300 K was maintained using a velocity-rescale thermostat, while semi-isotropic pressure control at 1 bar was ensured via a Berendsen pressure coupling scheme. Both NVT and NPT equilibration phases spanned 30 picoseconds under stable 300 K conditions.

Trajectory data from 200-ns MD simulations were evaluated to investigate system dynamics. The computational runs were executed via the Gromacs 2019.6 package47 (Van Der Spoel et al. 2005), with protein modeling based on the Amber 14SB force field. Key parameters including radius of gyration (Rg), Root mean square deviation (RMSD), hydrogen bonding variations, and solvent-accessible surface area (SASA) were systematically assessed throughout the simulation period.

Models of IFI204 and SENP7 were sourced from the Uniport Protein Data Bank (UPJNAR 2021). The structures of IFI204 and SENP7 were downloaded from AlphaFold2 (Jumper 2021). The results of the docking studies were processed using HDock (https://pubmed.ncbi.nlm.nih.gov/28521030/) and visualized with Pymol, with subsequent analysis conducted using LigPlot +.

The IFI204 model was obtained from the Uniport Protein Data Bank (UPJNAR 2021), while its structure was downloaded from AlphaFold2 (Jumper 2021). In the modeling results, the initial region of the protein, along with the area exhibiting high B-Factor flexibility and low accuracy, was removed. Molecules were sourced from the Zinc 20 (Zinc Drug Database) (Irwin 2020), selecting those with a molecular weight of less than 250 and a logP range of 1–5 for download. RDKit was utilized to read the small molecule structures, and the Descriptors module was employed to calculate indicators such as molecular mass, logP, and HIA, as well as to evaluate Lipinski and ESPSIM rules for screening purposes. Call the MMFOptimizeMolecule module through RDKit to optimize the structure and energy of molecules (under MMFF94) (Thomas and Robert 1996). Pocket prediction was conducted using ProteinPlus (Katrin 2020), and the docking process utilized smina software with a docking approximation degree of 20 (exhaustiveness), generating 20 conformations each time. Finally, PLIP was used to analyze the protein–ligand interaction results, while PyMOL 2.5.1 and LigPlot 2.1 were employed for visualization.

Statistical analysis

Statistical analyses were performed using GraphPad Prism software (version 8.4.3, GraphPad Inc., San Diego, USA). Quantitative data are presented as mean values ± standard error of the mean (SEM). Data normality and variance homogeneity were evaluated through Shapiro–Wilk and Brown-Forsythe tests, respectively. Datasets conforming to normality and equal variance were subjected to one-way ANOVA with Bonferroni's post hoc analysis. Behavioral metrics-specifically mNSS, rotarod performance, grip strength, and foot fault assessments-were analyzed via two-way repeated measures ANOVA with Bonferroni's post hoc test was conducted. Statistical significance was defined at $P < 0.05$. The statistical significance was defined as follows: $^{**}p < 0.01$, $^{***}p < 0.001$ as compared with the IFI204$^{f/f}$-Sham group or IFI204$^{f/f}$-Control group; $^{\#}p < 0.05$, $^{\#\#}p < 0.01$, $^{\#\#\#}p < 0.001$ as compared with the IFI204$^{f/f}$-TBI group or IFI204$^{f/f}$-OGD/R group; $^{\&}p < 0.05$ as compared with the IFI204 cKO-OGD/R group.

Results

Single-cell RNA-sequencing analysis identifies cell lineages in the subacute phase of the TBI

In order to assess the cellular heterogeneity during the subacute phase of TBI, specifically at seven days post-injury (dpi), One TBI-related scRNA-seq dataset (GSE160763) were analyzed utilizing an integrated bioinformatics approach. Our investigation focused on a control group, which comprised a total of 13,471 individual cells, and a TBI group that included 9,482 cells. Following quality control and filtration, cells from cortical were clustered into 15 unique cell clusters (Fig S1A). A total of 9 cell types were annotated according to their corresponding gene markers and were visualized:microglia (P2ry12, Tmem119, and Csf1r), astrocyte (F3, Aqp4, and Gja1), oligodendrocyte (Mog, Plp1, and Trf), neuron (Meg3, Rbfox3, and Rtn1), endothelial cell (Cldn5, Flt1, and Abcb1a), pericyte (Dcn, Lum, and Gsn), T cells (Cd3d, Cd3e), B cells (Cd79a, Ly6d, and Ms4a1) and smooth muscle cells (SMCs,Tagin, Acta2, and Myl9) (Fig. 1A-C). Cell proportion analysis indicated that microglia cells and astrocyte cells accounting for approximately 42% and 30% respectively in the control group, but the number of cells was approximately 50% in case of microglia cells and 17% in case of astrocyte cells in the TBI group (Fig. 1D and Fig S1B). The nine clusters encompassed all primary cell types identified at the TBI site, and the expression levels of the top six DEGs are shown in Fig. 1E. The differentially expressed genes across microglia, astrocytes, B cells, and T cells were acquired by comparing the Control and TBI groups and were visualized using the volcano plots (Fig S1C-F). Taken together, our results revealed significant alterations in major cell types between the normal group and the TBI injury group.

Dissection and clustering of microglia cells in cortical TBI samples

To better understand phenotypic heterogeneity on Day 7 after TBI, we performed further cluster analysis of microglia. In total, 10,441 cells were clustered into 7 separate subclusters (Fig. 2A). Significant differences in cell proportions were observed between the two groups. Specifically, the proportions of M0 and M1 cells decreased markedly after TBI, whereas

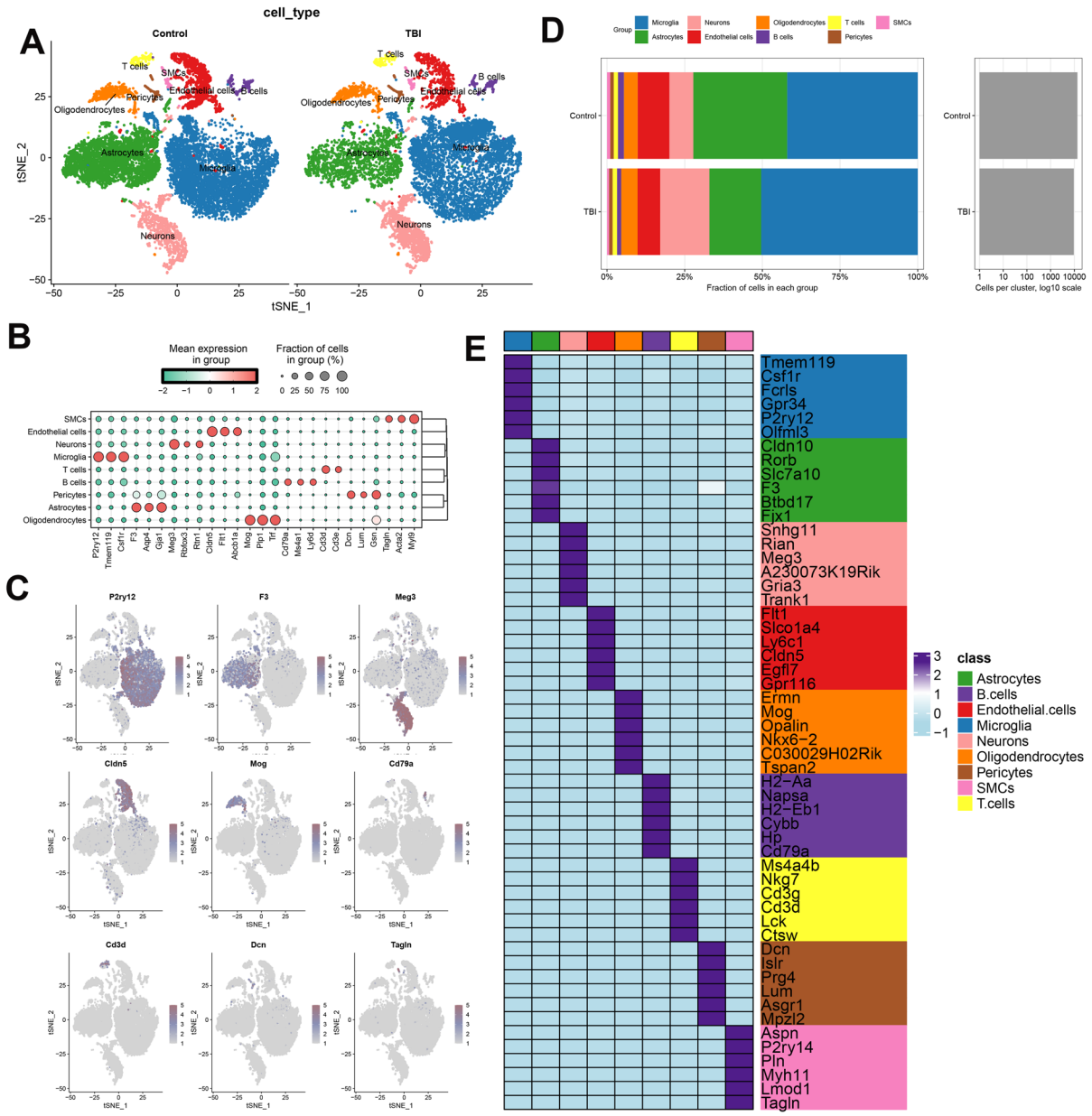

Fig. 1 Single-cell RNA-sequencing determines major cell types and cell type-specific genes in the cortex on Day 7 after TBI. **A** t-SNE plots illustrate the arrangement of various cell types in both control and TBI groups. Each colored dot corresponds to an individual cell. **B** Dot plot showing the expression of previously reported marker genes in nine cell types. **C** t-SNE visualizations emphasize the primary cell types based on marker gene expression. **D** Bar plot showing the fraction of each cell type in control and TBI group. **E** Heatmap showing the expression of the top six DEGs of each cell type

the proportions of M2 and M4 were increased in the microglia of the TBI group (Fig. 2B). In addition, MG0, MG1, and MG3 were identified as homeostatic microglia, characterized by the expression of markers of steady-state microglia, such as P2ry13, Selplg, Cx3cr1, Tmem119, and P2ry12. MG5 was distinguished by the increased expression of inflammation-related genes, including Ccl3, Ccl4, Ccrl2, Nfkbia, Osm, Socs3, and Zfp36. MG6 showed high expression of Atp1b2, Ptprz1, Ptn, and Gpm6b, which are

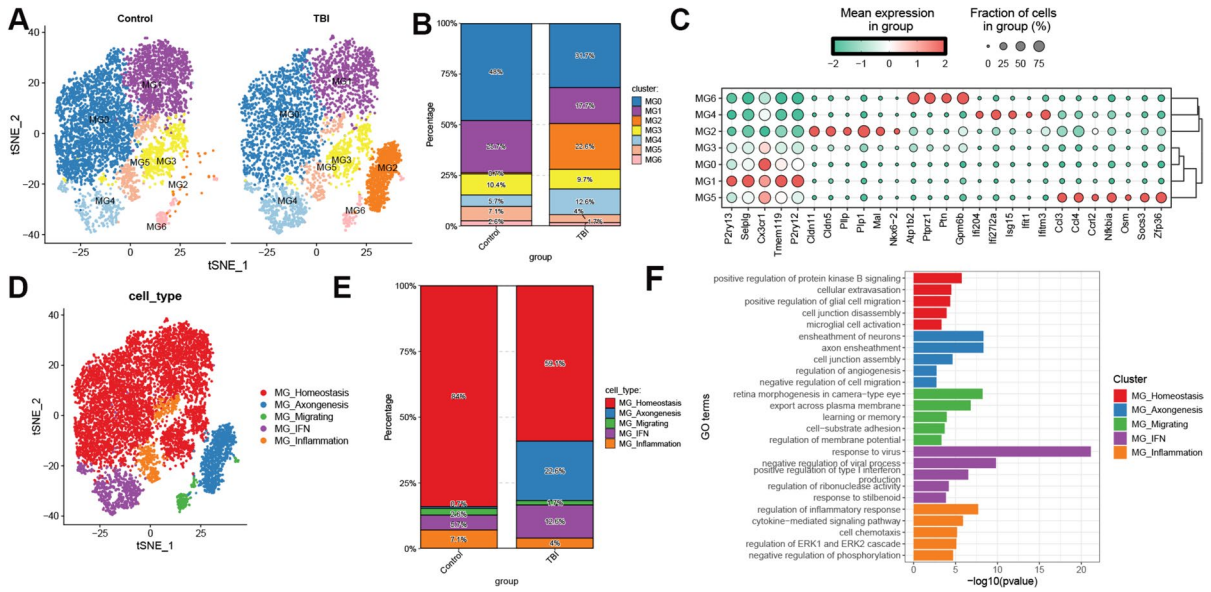

Fig. 2 Molecular profile of microglia subset phenotypic heterogeneity on Day 7 after TBI. **A** t-SNE plots showing the distribution of various microglia clusters in both control and TBI groups. Each colored dot corresponds to a microglia subcluster. **B** Bar plot showing the fraction of each microglia subcluster between control and TBI groups. **C** Dot plot showing the expression of conserved marker genes in seven microglia subclusters. **D** t-SNE plot showing the distribution of defined microglia subtypes. **E** Bar plot showing the fraction of each defined microglia subtype between control and TBI groups. **F** Enrichment analysis of the biological function across each cell types. biological process terms displayed along y axis, and $-\log_{10}$ (*P* values) displayed along x axis

closely associated with cell migration. MG2 demonstrated an increased expression of axonogenesis-related genes, such as Cldn11, Cldn5, Pllp, Plp1, and Mal. Furthermore, in MG4, the elevated expression of interferon-related genes, including Ifi204, Ifi2712a, Isg15, Ifit1, and Ifitm3, was also observed (Fig. 2C, D). In the control group, homeostatic, axonogenesis, and IFN microglia accounted for approximately 84%, 0.7%, and 5.7%, respectively. However, in the TBI group, the proportion of homeostatic microglia decreased to 59.1%, while the proportions of axonogenesis and IFN microglia increased to 22.6% and 12.6%, respectively (Fig. 2E). Analysis of biological function enrichment showed that inflammatory microglia were mainly connected to pathways related to cell chemotaxis and cytokine-mediated signaling, while migrating microglia were associated with processes of cell migration and adhesion. Axonogenesis microglia predominantly pertained to axon ensheathment. Furthermore, IFN-related microglia exhibited a strong enrichment for viral interactions. In contrast, revealed specific enrichment for biological function related to microglial cell migration and cellular extravasation (Fig. 2F). Subsequently, we performed differential expression analysis on microglia and astrocytes in both the Control and TBI groups. Compared to the control group, the expression of multiple interferon-related genes (Ifi27 l2a, Ifitm3, and Ifi204) in microglia of the TBI group was significantly increased, and these genes ranked relatively high among all upregulated genes (Fig S1D). In addition, we found Ifi204 was highly expressed in microglia relative to astrocyte, neuron, endothelial cell, and was significantly higher than the Control group after TBI (Fig. S2). For these reasons, Ifi204 was selected for further analysis. In summary, our findings indicate that several distinct cellular states within the microglia undergo a temporal evolution. Notably, this progression moves towards a more non-steady-state condition on Day 7 after TBI.

Transcriptional trajectory of microglia cells

To investigate the origin of microglial cells in the occurrence of brain injury on day 7 after TBI, trajectory analysis was carried out based on the five unique

cell types. A total of seven different differentiation states and three independent branch points were finally determined. The migrating microglia cells appeared at the beginning of the trajectory. Steady-state microglia were mainly located in the center, while the inflammation, IFN and axonogenic microglia cells appeared at the trajectory ends (Fig. 3A-C). Notably, with the development of brain injury, the migrating microglia population is divided into two unique branches, suggesting the internal heterogeneity of these microglia. Subsequently, the identified 1182 differentiation-related genes utilizing pseudotime trajectory analysis were further clustered into 3 subgroups (Fig. 3D). Among them, the expression of genes associated with microglial IFN and inflammation response in the C1 subgroup, such as Ccl3, Ccl4, lfi204, and Isg15, were gradually increased during the progression of brain injury. Consistently, as pseudochron progression, the enhanced expression of genes related to microglial axonogenesis (Cldn5, Cldn11, Mal, Nkx6-2, Plp1, Pllp) and IFN microglia (lfitm3, Oasl2 and lfit1) in the C2 pattern were also observed. In addition, genes enriched in the C3 pattern and closely related to microglial migration, including Atp1b2, Ptn, and Ptprz1, increased at the start of trajectory and gradually decreased as

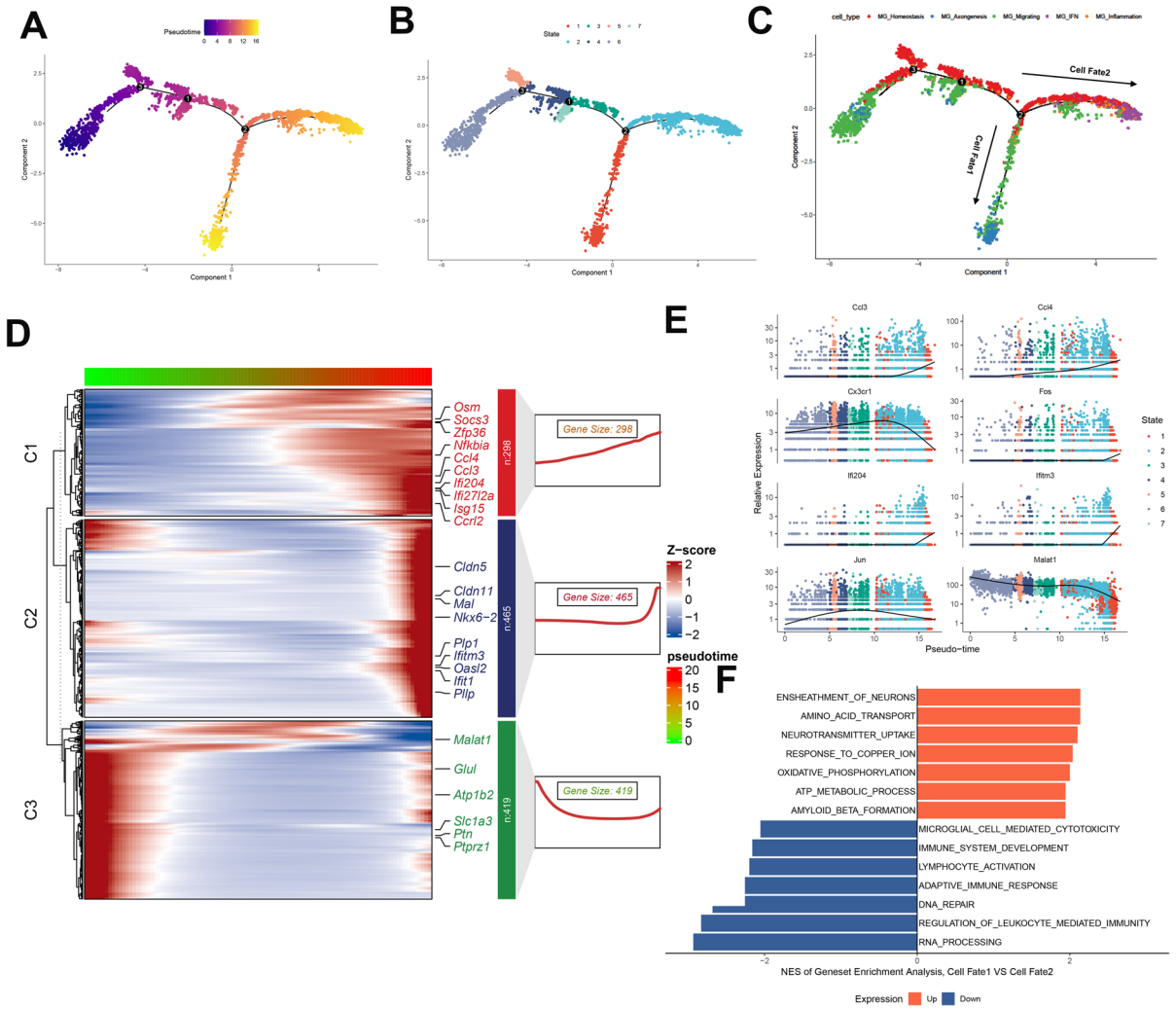

Fig. 3 Trajectory analysis of microglia. **A-C** Trajectory plots show the differentiation of these cell types. **D** Heatmap of different blocks of marker genes throughout the pseudotime trajectory. **E** Dynamic gene expression with pseudotime trajectory. **F** GO functional enrichment analyses in Fate1 and Fate 2 cell fate transitions

the disease progressed (Fig. 3C, D). Subsequently, we evaluated the underlying mechanisms of this heterogeneity of pseudotime trajectory. Estimating the activity of known pathway members in IFN and axonogenic microglia populations indicated that metabolism- and transport-related biological functions were mainly enriched in cell fate 1. Strikingly, cell fate 1 also showed specific enrichment of biological functions associated with Aβ formation and the response of Cu^{2+}. However, immune-induced pathways were predominant increased in cell fate 2 (Fig. 3E, F). Collectively, these findings revealed that the existence of these activated microglia could contribute to the progression of TBI.

TBI induced astrocyte dissection and clustering

To better understand phenotypic heterogeneity on Day 7 after TBI, we performed further cluster analysis of astrocyte. Further analysis of astrocyte revealed four (AST1–4) cell clusters (Fig. 4A). Then, we defined these clusters as different astrocyte states according to their marker genes and molecular functions. The oxidative phosphorylation (OXPHOS)-related astrocyte (AST0) was annotated due to the significant enrichment of ATP generation (Chchd10, Cox5a, Cycs, and Nupr1). We also found two reactive states (AST1 and AST2) showing high expression of several catabolic process (Apoe, Cd81, Clu, Gja1, Pla2 g7, and Psap) and strong functional enrichment in cell chemotaxis and neuron death. Therefore, AST1 was annotated as reactitivity1 (Apoe and Clu) and AST2 was defined as reactitivity2 (Enpp2, Padi2, Plec, and Thbs4). In addition, AST3 exhibited apparent enrichment of neurogenesis and neuron differentiation (Fig. 4B-D). These results reveals novel subsets and myriad functions of astrocytes at 7 dpi after TBI.

Transcriptional trajectories of astrocyte

To investigate the impact of TBI on the evolution of astrocyte subsets, we analyze, the cortical samples of mice subjected to brain injury at 7 dpi or in the control condition with trajectory analysis. The results determined one independent branch point (Fig. 5A). The synapse astrocyte appeared at the beginning of the trajectory, OXPHOS and reactivity2 astrocyte gradually increased, and the reactivity1 astrocyte appeared at the end of the trajectory (Fig. 5B). Next, we performed volcano plots for the DEG expression of the synapse and reactivity1 astrocyte (Fig. 5C). There were numerous genes significantly increased in synapse astrocyte including lgfbpl1, Sox4, Stmn1, Tmsb10, and Tubb5, whereas Atp1a2, Gpr37 l1, Mfge8, Slc7a10, Gnn2c and Hltra1 were significantly downregulated. Enrichment analysis of DEGs along the pseudotime trajectory revealed that cytoplasmic translation, ribonucleoprotein complex biogenesis, subunit organization, comp assembly, and ribosome biogenesis were positive enrichment at the initial stage. Subsequently, it evolved into the biosynthetic processes of carboxylic acids and organic acids, as well as mechanisms for detoxification and responses to zinc ions and toxic substances. At the end of progression, signaling pathway, including glial cell differentiation, gliogenesis, amino acid import across plasma membrane, steroid metabolic process and L-alpha-amino acid transmembrane transport (Fig. 5D). Subsequently, the findings derived from the DEG-based functional analysis were validated through the implementation of GSEA. The results revealed Lipid metabolic process signaling pathway was significantly enriched in reactivity1 astrocyte. However, synapse astrocyte was mainly enriched in cytoskeleton organization (Fig. 5E, F). The gene expression pattern across pseudotime showed that the expression curves of Dkk3 were relatively smooth (Fig. 5G). These results revealed that astrocyte followed a differentiation trajectory that primarily began with clusters of synapse astrocyte, from which they differentiated into reactivity1 astrocyte.

Microglial IFI204 knockout ameliorates TBI-induced neurological functions deficit in mice

To investigate the role of IFI204 in a living organism, we created inducible IFI204 microglia-specific knockout mice, referred to as IFI204 cKO mice. The absence of IFI204 in microglia was verified through Western Blot analysis (Fig. 6A, B). Figures 6B illustrate that the cKO mice exhibited significantly lower levels of IFI204 in comparison to the $IFI204^{f/f}$ mice. We conducted several tests, including evaluation of mNSS scores, rotarod test, grip force test, and foot fault tests before and after TBI at different time points (1 d, 3 d, and 7 d), to evaluate the usefulness of IFI204 cKO in the mouse model of TBI. The mNSS scores indicated that treatment

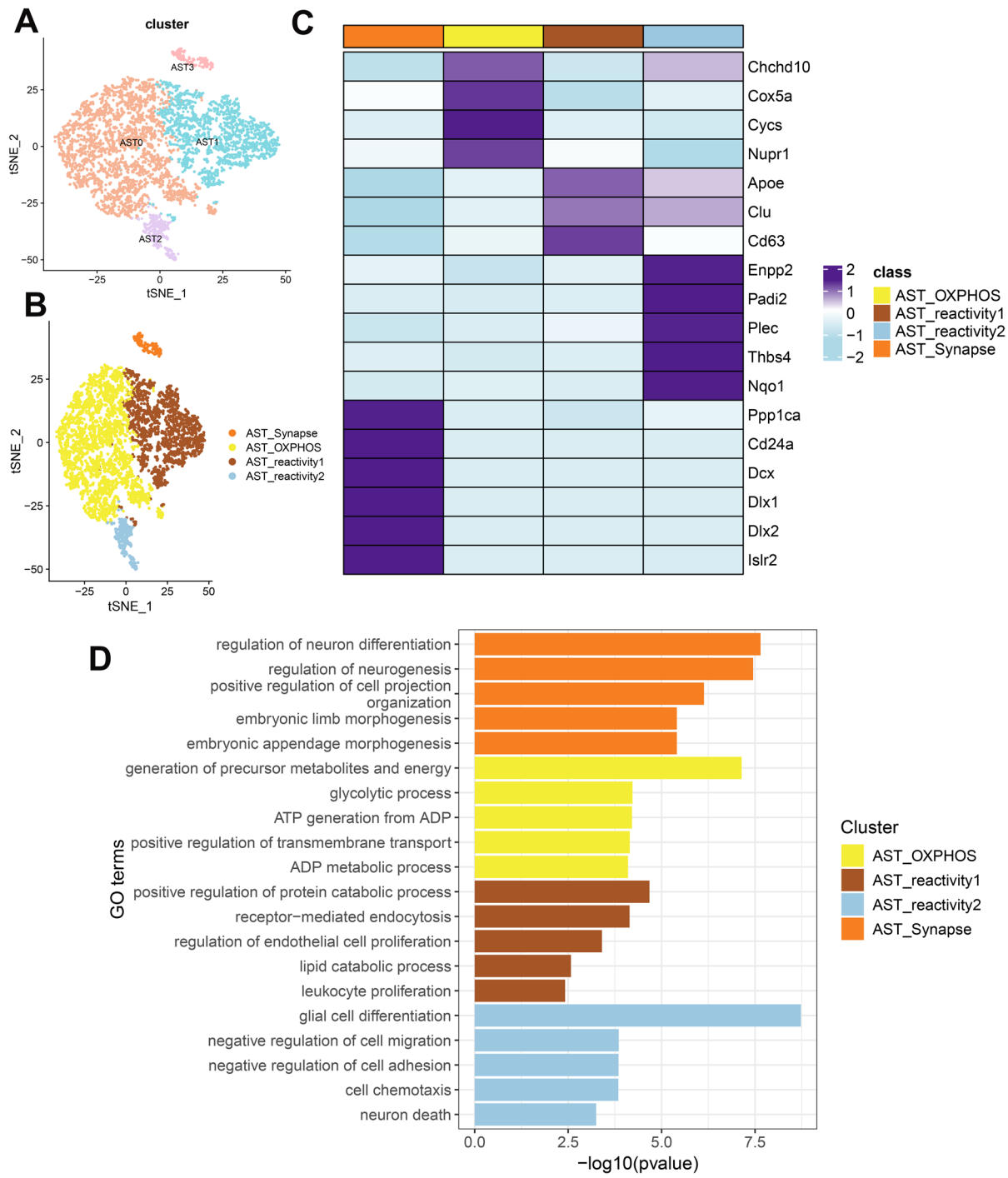

Fig. 4 Molecular profile of astrocyte subset phenotypic heterogeneity on Day 7 after TBI. **A** A t-SNE plots of astrocyte clusters. Each colored dot represents astrocyte subcluster. **B** Subcluster of astrocyte showing four subsets. **C** Heatmap of the Marker genes per astrocyte subset. Color represents z-score expression level. **D** Analysis of GO enrichment for the marker genes in each subset. The biological process terms of GO are represented on the y-axis, while the –log10 (*P* values) are shown on the x-axis

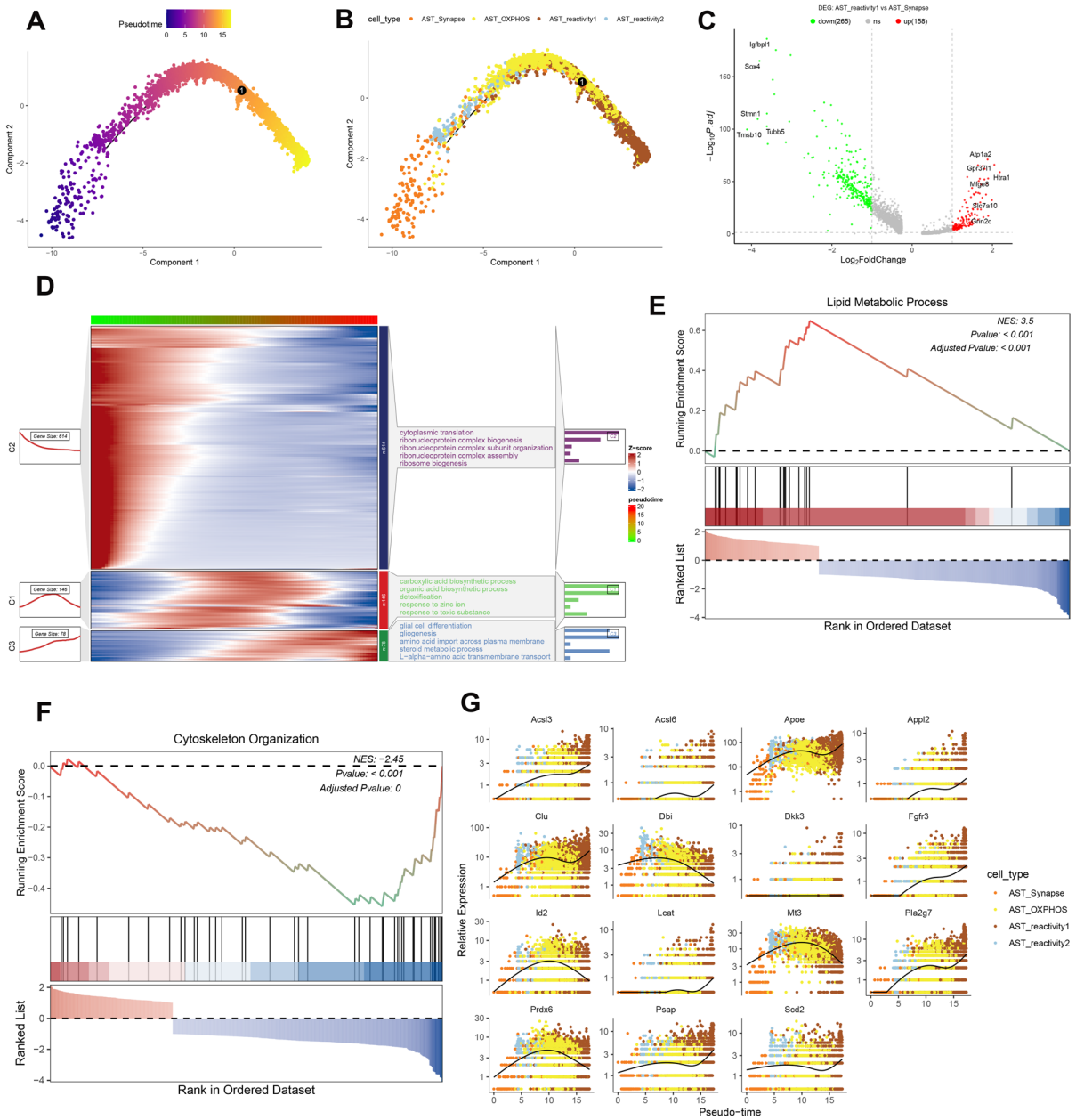

Fig. 5 Developmental trajectories of astrocyte. **A-B** Monocle2 analyses show the development of astrocyte. **C** Volcano map of DEGs between the pseudotime trajectory in reactivity1 and Synapse astrocyte. **D** Heatmap of GO functional enrichment analyses of different clusters (C1-C3) along the pseudotime trajectory. **E** Representative GSEA plots for a lipid metabolic process. **F** Representative GSEA plots for the cytoskeleton organization. **G** Dynamic gene expression with pseudotime trajectory

with IFI204 cKO effectively mitigated neurobehavioral deficits at 1 d and 7 d post-TBI, compared to the IFI204$^{f/f}$-TBI group (Fig. 6C). Similarly, mice in the IFI204 cKO-TBI group exhibited significantly longer duration on the rotarod at 7 d, compared to the IFI204$^{f/f}$-TBI group (Fig. 6D). Likewise, the grip strength assessment demonstrated enhanced grip force in the IFI204 cKO-TBI group at 1 d,

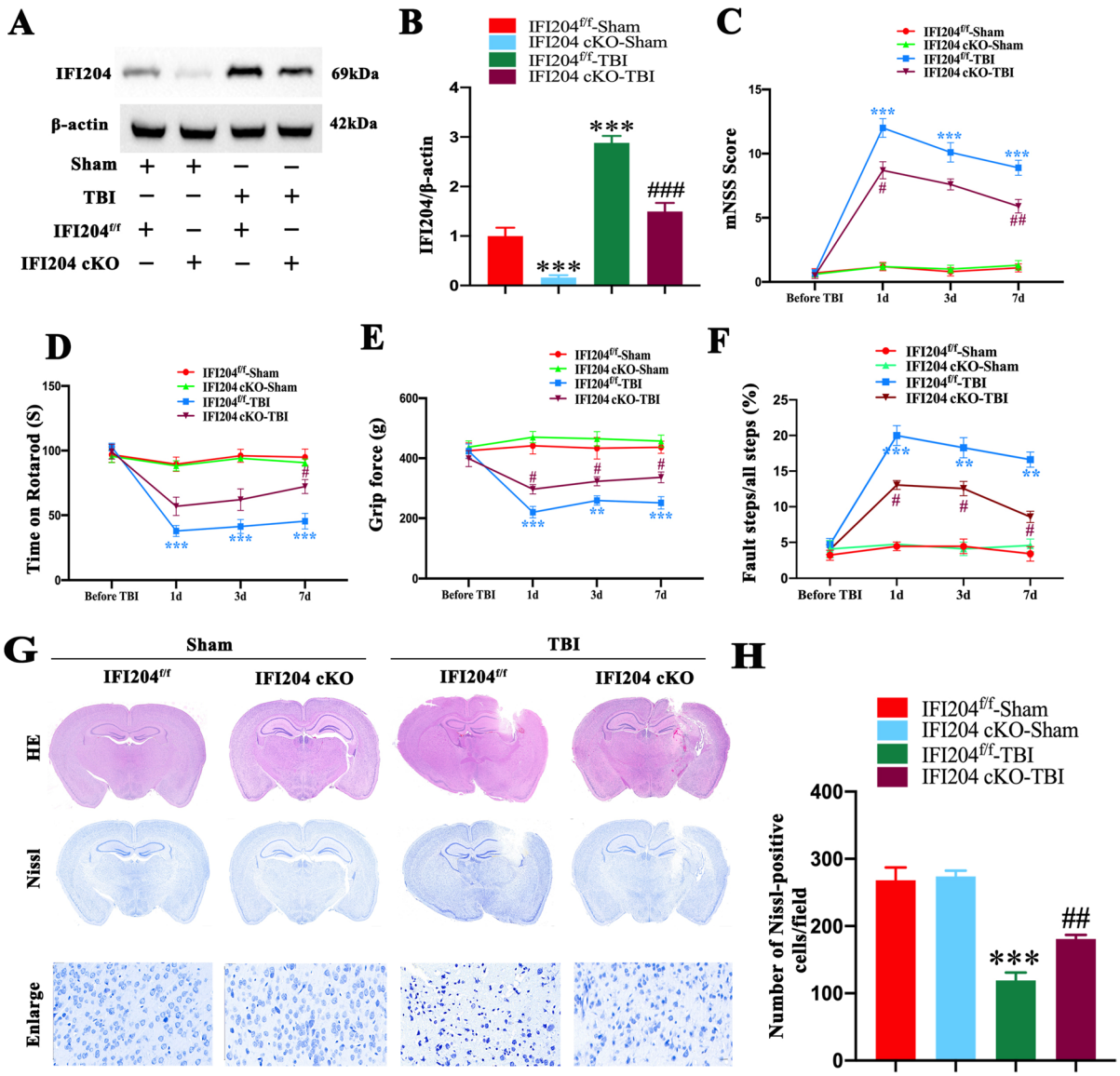

Fig. 6 The improved neurological functional recovery by IFI204 knockout after TBI. **A** Representative immunoblots and (**B**) Western Blot analysis of IFI204 in the cortical region of different groups; $n = 3$. **C** Modified neurological severity scores (mNSS), (**D**) Rotarod test, (**E**) Grip force test, (**F**) The forepaw foot fault assessment was conducted in various groups prior to TBI and at 1 day, 3 days, and 7 days following TBI; $n = 10$. **G** Representative images of different groups by Nissl, HE staining at 7 days after TBI; Scale bar = 20 μm. **H** Quantitative analysis of Nissl-positive cells; $n = 3$

3 d, and 7 d, when compared to the grip strength observed in the IFI204$^{f/f}$-TBI group (Fig. 6E). Compared to the IFI204$^{f/f}$-TBI group, the IFI204 cKO-TBI group exhibited a reduction in the number of forepaw fault steps in the foot fault test at 1 d, 3 d, and 7 d (Fig. 6F). Further, using Nissl and HE staining, we found that the brain coloboma was markedly decreased in IFI204 cKO mice in comparison to the IFI204$^{f/f}$ group at 7 d after TBI (Fig. 6G). Nissl staining revealed that, compared to the sham-operated group, the number of Nissl-positive stained cells in mice after brain injury decreased, and the neuronal survival rate significantly declined. IFI204 cKO treatment significantly increased the number

of Nissl-positive stained cells and improved the neuronal survival rate (Fig. 6H). Overall, these findings suggest that microglia specific deletion of IFI204 attenuates sensorimotor deficits and tissue loss in mice after TBI.

Microglial IFI204 knockout attenuates TBI-induced mitochondrial structure and function damage in mice

To further understand the impact of IFI204 knockout on mitochondrial structure and function, we evaluated various mitochondria-related biochemical markers. The findings revealed elevated levels of MDA and reduced activity of SOD, as well as a decline in the GSH/GSSG ratio and GSH-Px activity in the IFI204$^{f/f}$-TBI group compared to the IFI204$^{f/f}$-Sham group. However, the IFI204 cKO mice maintained optimal levels of SOD, GSH/GSSG, and GSH-Px, and significantly suppressed MDA production when compared to the IFI204$^{f/f}$-TBI group (Fig. 7A-D). Given the essential role of ROS in injury caused by TBI, we further examined how IFI204 influences resistance to oxidative stress. The results demonstrated a substantial rise in ROS production in the IFI204$^{f/f}$-TBI group and IFI204$^{f/f}$-OGD/R group. However, the IFI204 cKO mice exhibited a notable decrease in ROS levels in the cortical tissue 7 days after TBI and in cultured microglia after OGD/R (Fig. 7E-G). Next, changes in mitochondrial morphology in vitro were visualized using confocal microscopy. Under normal conditions, microglial cells predominantly display elongated tubular mitochondria. In contrast, 24 h post-OGD/R injury, the mitochondrial structure of the majority of microglial cells appeared to be nearly entirely fragmented in comparison to the IFI204$^{f/f}$-Control microglial cells. However, the IFI204 cKO-OGD/R group mice significantly reduced the rate of mitochondrial fragmentation and alleviated OGD/R-induced mitochondrial damage (Fig. 7H). The analyses indicated that OGD/R led to a notable reduction in the ratio of JC-1 aggregates (red fluorescence) to JC-1 monomer (green fluorescence) in cultured microglia. In contrast, the IFI204 cKO-OGD/R group relieved this membrane depolarization when compared to the IFI204$^{f/f}$-OGD/R group (Fig. 7I, J). Overall, these results suggest that the IFI204 cKO mitigates oxidative stress damage and mitochondrial network fragmentation following TBI.

Microglial IFI204 knockout attenuated TBI-induced microglial pyroptosis in mice

To assess if the knockout of IFI204 suppressed pyroptosis following TBI, we analyzed the expression levels of pyroptosis-related proteins by Western blot. As illustrated in Fig. 8A, the levels of the pyroptosis-associated proteins were markedly elevated post-TBI, and remarkably blocked by IFI204 cKO mice in comparison with IFI204$^{f/f}$-TBI mice. To further evaluate the precise role of IFI204 in microglial pyroptosis in a laboratory setting, we conducted OGD/R injury experiments. RT-PCR results show that IFI204 cKO group decreased IL-1β and IL-18 secretion (Fig. 8B, C). In a similar fashion, the GSDMD, GSDMD-N, Pro caspase-1, Caspase-1 p20 protein upregulation induced by OGD/R injury were reversed in IFI204 cKO microglia (Fig. 8D). Immunofluorescence analysis revealed that treatment with IFI204 cKO led to a considerable reduction in the average fluorescence intensity of GSDMD-positive microglia following OGD/R injury (Fig. 8E, F). Collectively, these results suggest that IFI204 cKO can reduce TBI-induced microglial pyroptosis and inhibit inflammatory activation.

The simulations of molecular dynamics and SENP7-mediated IFI204 deSUMOylation after OGD/R

Our subsequent aim was to investigate if SENP7 facilitates deSUMOylation in the regulation of IFI204. Initially, we verified whether IFI204 is subject to modification through SUMOylation. CO-IP assays demonstrated that the IFI204 can be conjugated by SUMO2/3 and SUMOylation of IFI204 was obviously decreased in cortical tissue after OGD/R (Fig. 9A). We examined whether SENP7 interacts with IFI204. The CO-IP assay further indicated that the natural interaction between SENP7 and IFI204 was significantly increased in cells following OGD/R (Fig. 9B). Taken together, these findings imply that SENP7 interacts with IFI204 and facilitates the deSUMOylation of IFI204 after OGD/R.

Molecular dynamics simulations (MDS) represent an essential technique for exploring for investigating the structural equilibrium and dynamic behavior of molecular complexes in aqueous systems. The RMSD of atomic positions provides a critical

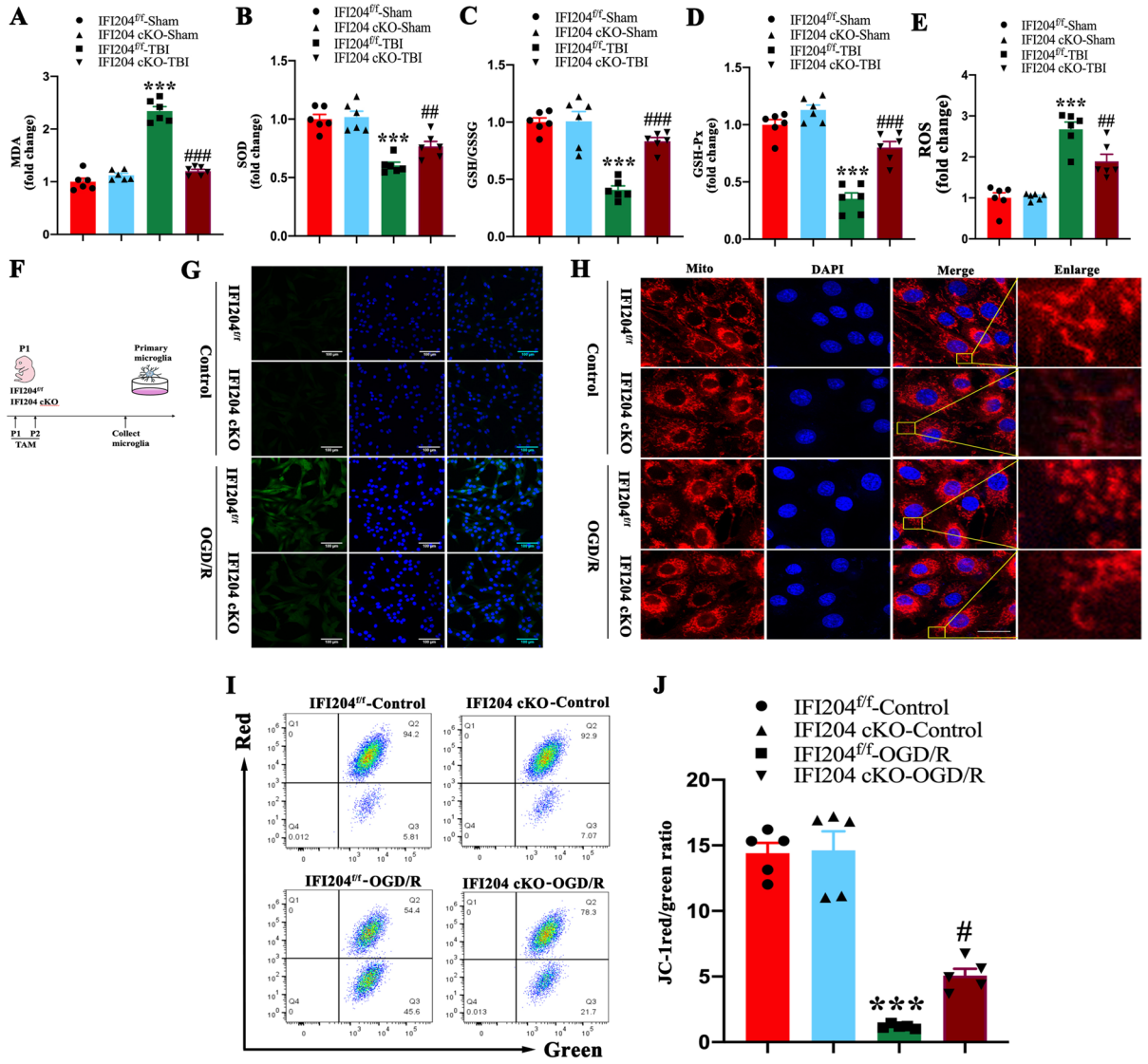

Fig. 7 The attenuated mitochondrial function injury and mitochondrial network fragmentation by IFI204 cKO after TBI. **A** Expression levels of MDA, (**B**) SOD, (**C**) GSH/GSSG, (**D**) GSH-Px, (**E**) ROS in the cortical tissues of different groups; $n = 6$. **F** A diagram illustrating the timeline of experiments conducted for the analysis of microglial cultures. **G** Measurement of ROS levels in cells of different groups using ROS detection reagent. **H** Depicted are representative confocal images highlighting the mitochondrial structures across various experimental groups. Scale bar = 20 μm. **I** Flow cytometry of JC-1 expression and (**J**) Quantified results of red/green in cultured microglial of different groups; $n = 5$

metric for assessing system stability. During the initial 60-ns simulation period, all analyzed systems exhibited consistent structural integrity, with RMSD values maintained at approximately 5.0 nm (Fig. 9C). The fluctuations in Fig. 9D correspond precisely to the twists and turns in the RMSD. Notably, Rg first decreases and then increases, indicating that the protein undergoes a contraction followed by a relaxation phase. Analyzing the trajectory reveals that certain structures of the complex protein exhibit relative freedom of movement, suggesting an outward expansion trend during the simulation. The root mean square fluctuation (RMSF) illustrates the movement state of each residue in the protein, showing that the first 200 residues exhibit significant mobility, indicating a trend of movement in this region (Fig. 9E). The

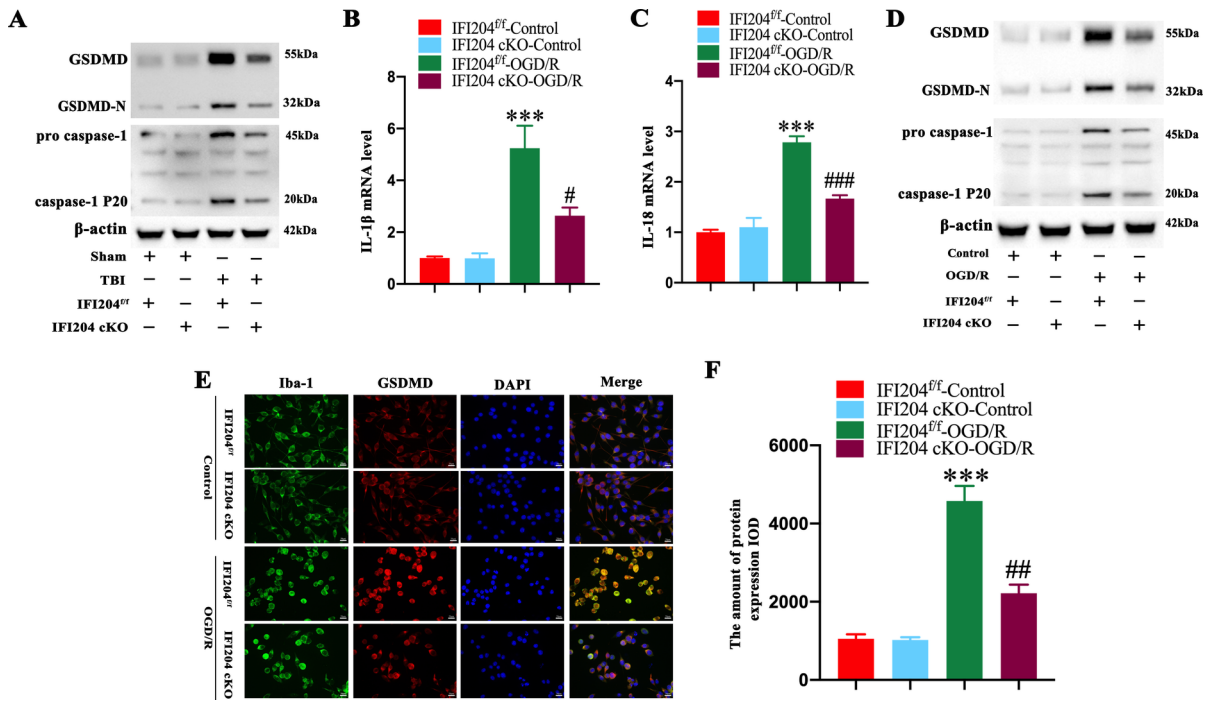

Fig. 8 The inhibition of TBI-induced microglial pyroptosis and inflammatory activation by IFI204 knockout. **A** Representative immunoblots of GSDMD, GSDMD-N, Pro caspase-1and Caspase-1 p20 protein in the cortical region of different groups. **B** RT-PCR analysis of IL-1β levels in microglia cells. $n = 4$. **C** RT-PCR analysis of IL-18 levels in microglia cells. $n = 4$. **D** Representative immunoblots of GSDMD, GSDMD-N, Pro caspase-1and Caspase-1 p20 protein in microglia 24 h post-OGD/R injury of different groups. **E, F** Immunofluorescence staining of GSDMD and Iba-1 in different groups and quantitation of signals. $n = 3$. Scale bar = 20 μm

SASA reflects the protein's surface exposure to solvent. It was observed that SASA steadily decreased from 0 to 100 ns, suggesting advantageous binding and a gradual tightening of the protein structure; however, some residues moved outward, resulting in a slight overall increase in surface area (Fig. 9F). The hydrogen bond change curve indicates that as the simulation progresses, the protein contracts, leading to a decrease in hydrogen bonds between the protein and water (Fig. 9G), while hydrogen bonds between protein molecules increase (Fig. 9H). By analyzing the conformation during docking, the interaction between the two proteins can be examined. Figure 9I illustrates that the two proteins possess a broad contact surface. The IFI204 protein envelops the SENP7 protein, with the beta-sheet of the SENP7 head embedded within the loop of the IFI204 head. Additionally, the head of IFI204 exhibits a swinging motion throughout the simulation process. The contact fingerprint was additionally illustrated to reflect the characteristics and force of the contact (Fig. 9J). Following the calculation of binding free energy for protein–protein complexes, we proceeded to evaluate the variation in binding free energy between two solvents containing the same proteins, considering both their bound and unbound states. Furthermore, we conducted a comparison of the free energy associated with different solvation conformations of the same molecule (Fig. 9K). Our analysis of the binding free energy changes using MDS revealed that the total free energy values were negative, indicating a strong likelihood of interaction between the proteins. Breaking this down into individual components, total gas phase free energy (GGAS) denotes the free energy of the gas phase, originating from the van der Waals energy (VDWAALS), and it is likewise negative. Specifically, a negative VDWAALS value suggests that hydrophobic interactions facilitate binding. Additionally, electrostatic energy (EEL), which represents electrostatic interactions, is negative as well, further

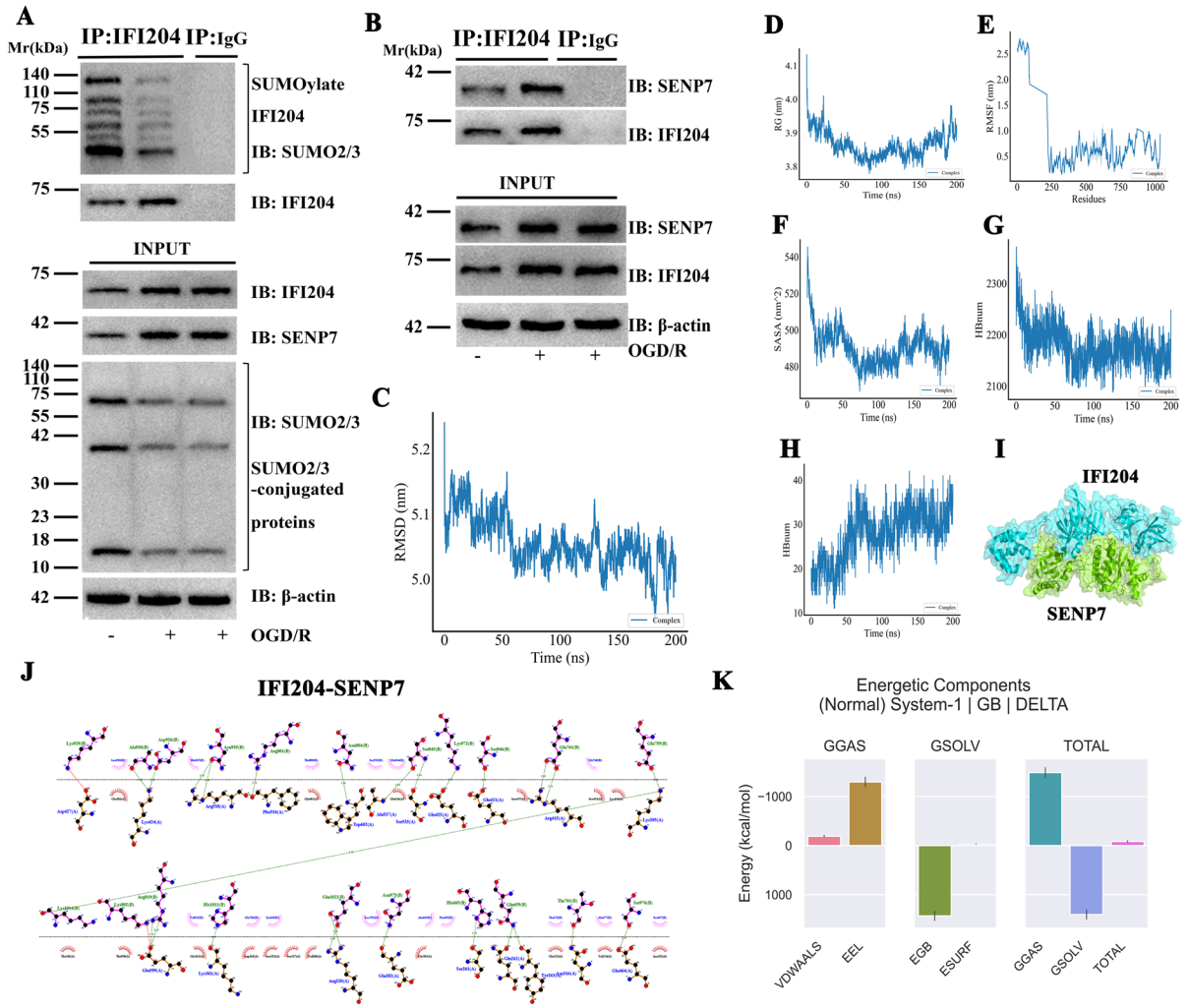

Fig. 9 The analysis of MDS results. **A** The SUMOylation of endogenous IFI204 in cortical tissue treated with OGD/R or not was examined by co-IP assay. **B** The interaction of ectopically expressed IFI204 with SENP7 was determined by co-IP. **C** RMSD. **D** Rg. **E** RMSF. **F** SASA and **G, H** hydrogen bond (HB) profiles of the IFI204 with SENP7. **I** The binding mode of IFI204 with SENP7. **J** The particular perspectives regarding the 2-D interaction of the ligand IFI204 with SENP7. **K** Distribution of complex free energy (kcal/mol) (A = IFI204, B = SENP7). TOTAL: GSOLV + GGAS

supporting the notion that these interactions are beneficial for binding. On the other hand, the overall solvation free energy, represented as total solvation free energy (GSOLV), has a positive value, suggesting that binding is not favorable. GSOLV is influenced by the interplay between non-polar solvation energy (ESURF) and polar solvation energy (EGB). The positive value of EGB implies that polar solvation is detrimental to binding, while non-polar interactions are favorable. These interactions demonstrate the strong links between IFI204 and SENP7.

IFI204 deSUMOylation boosts the STING signaling pathway in microglia following OGD/R

To investigate the role of SENP7 in OGD/R, we utilized lentiviral (LV) vectors to knockdown SENP7 expression in microglia. Additionally, we employed DMXAA, a pharmacological activator of STING, to assess the effects of STING on microglial pyroptosis in cultured cells. Our results indicated a significant increase in p-TBK1, p-STING, GSDMD, GSDMD-N, Pro-caspase-1 and caspase-1 p20

levels in the IFI204$^{f/f}$-OGD/R group compared to the IFI204$^{f/f}$-Control group. Conversely, a notable reduction in the levels of these proteins was noted in the IFI204 cKO-OGD/R and IFI204$^{f/f}$-LV-sh_SENP7-OGD/R group relative to the IFI204$^{f/f}$-OGD/R group. Furthermore, the IFI204 cKO-OGD/R-DMXAA group showed significantly elevated levels of p-TBK1, p-STING, GSDMD, GSDMD-N, Pro-caspase-1 and caspase-1 p20 compared to the IFI204 cKO-OGD/R group (Fig. 10A). Immunofluorescence analysis revealed that LV-sh_SENP7 treatment led to markedly reduced mean fluorescence intensity values for GSDMD-positive microglia following IFI204$^{f/f}$-OGD/R injury, DMXAA reverses this phenomenon (Fig. 10B, C). RT-PCR results show that IFI204$^{f/f}$-LV-sh_SENP7 decreased IL-1β and IL-18 secretion, DMXAA reverses this phenomenon (Fig. 10D, E). Collectively, these results indicate that IFI204 deSUMOylation enhances the STING signaling pathway in microglia after OGD/R.

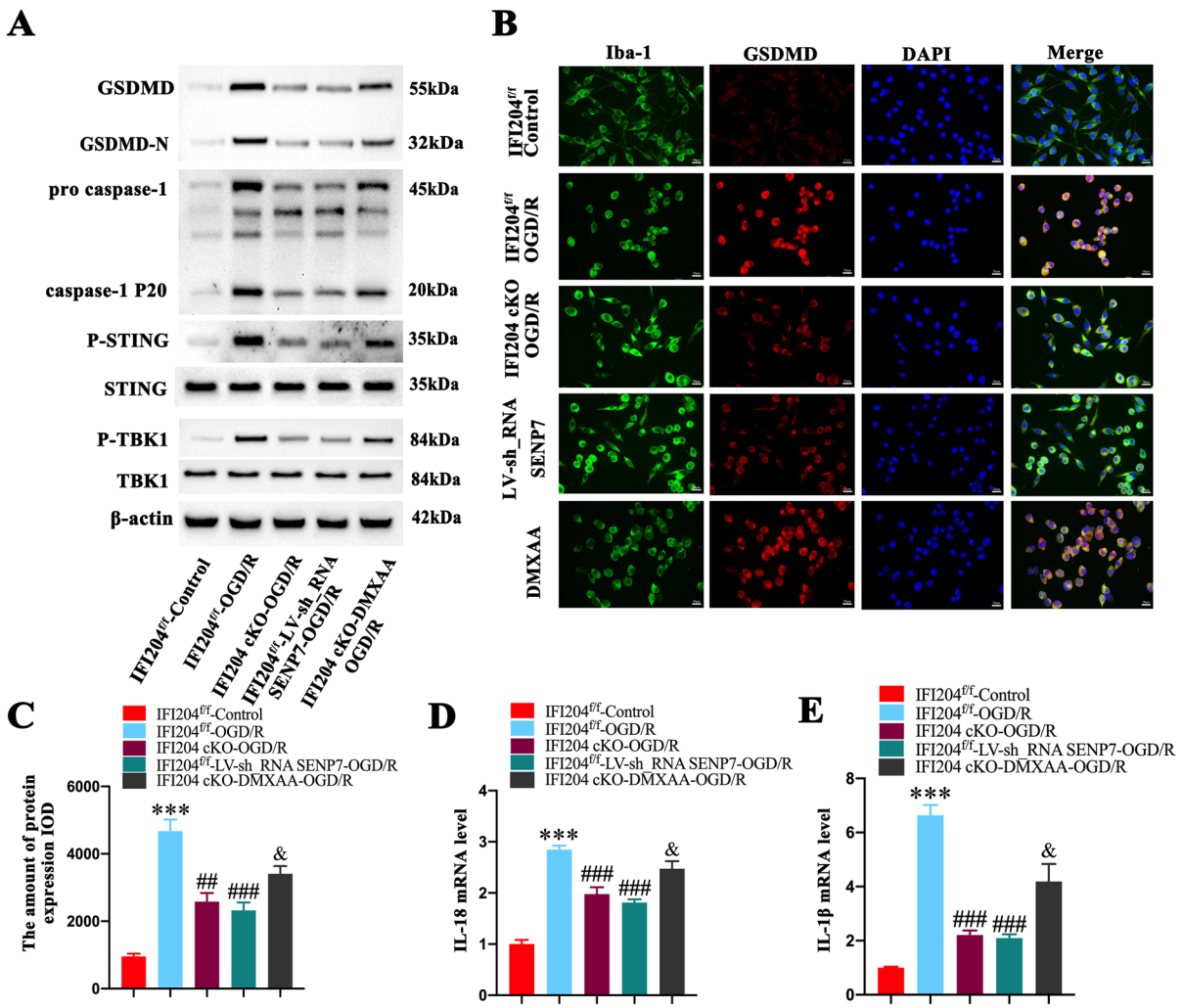

Fig. 10 The inhibition of TBI-induced STING signaling pathway by IFI204 knockout. **A** Representative immunoblots of GSDMD, GSDMD-N, p-TBK1, p-STING, GSDMD, GSDMD-N, Pro caspase-1and caspase-1 p20 protein in microglia 24 h post-OGD/R injury of different groups; **B** Immunofluorescence staining of GSDMD and Iba-1 in different groups and (**C**) quantitative analysis. $n = 3$. Scale bar: 20 μm. **D** RT-PCR analysis of IL-18 levels in microglia cells. $n = 4$. **E** RT-PCR analysis of IL-1β levels in microglia cells. $n = 4$

IFI204 stably binds to small molecule compounds

We initially identified 17,936,637 molecule compounds (Fig. 11 A). To expedite the process, we eliminated certain molecules with particularly poor scores, ultimately narrowing our selection to 1,048,575 molecules. We selected the top 5%, resulting in a total of 6,005,501 molecules (Fig. 11 B). Next, we will use ProteinPlus for protein pocket prediction. Figure 11 C presents the results of the protein pocket prediction, where the yellow and purple regions in the center indicate potential pockets. Their volumes are 1304.1 and 1143.82 Å^3, and the inner surface areas of the pockets are 1758.15 and 1326.54 Å^2. These two pockets are candidates for docking. Subsequently, we utilized smina software to perform molecular docking and assess the binding energy between the compound and the core target to predict their affinity. A more negative binding energy value suggests greater stability of the conformation. In Fig. 11 D, it is evident that molecule compound resides in the middle-left pocket of IFI204, forming hydrophobic interactions with PRO-528, ALA-526, and LYS-420, as well as π-π stacking interactions with TYR-532. The docking score for this interaction is −8.2 kcal/mol. Figure 11 E illustrates that the molecule compound stays in the middle-left pocket of IFI204, forming hydrophobic interactions with PRO-528, TYR-532, THR-540, and GLU-421, and establishing hydrogen bonds with LYS-424 and GLN-536, yielding a docking score of −8.0 kcal/mol. Figure 11 F further demonstrates that molecule compound stays in the middle-left pocket of IFI204, forming hydrophobic interactions with PRO-528, TYR-532, LYS-420, and GLU-421, while also forming hydrogen bonds with ARG-523. The docking score for this interaction is −7.9 kcal/mol. These results indicate that molecule compounds can effectively bind to key

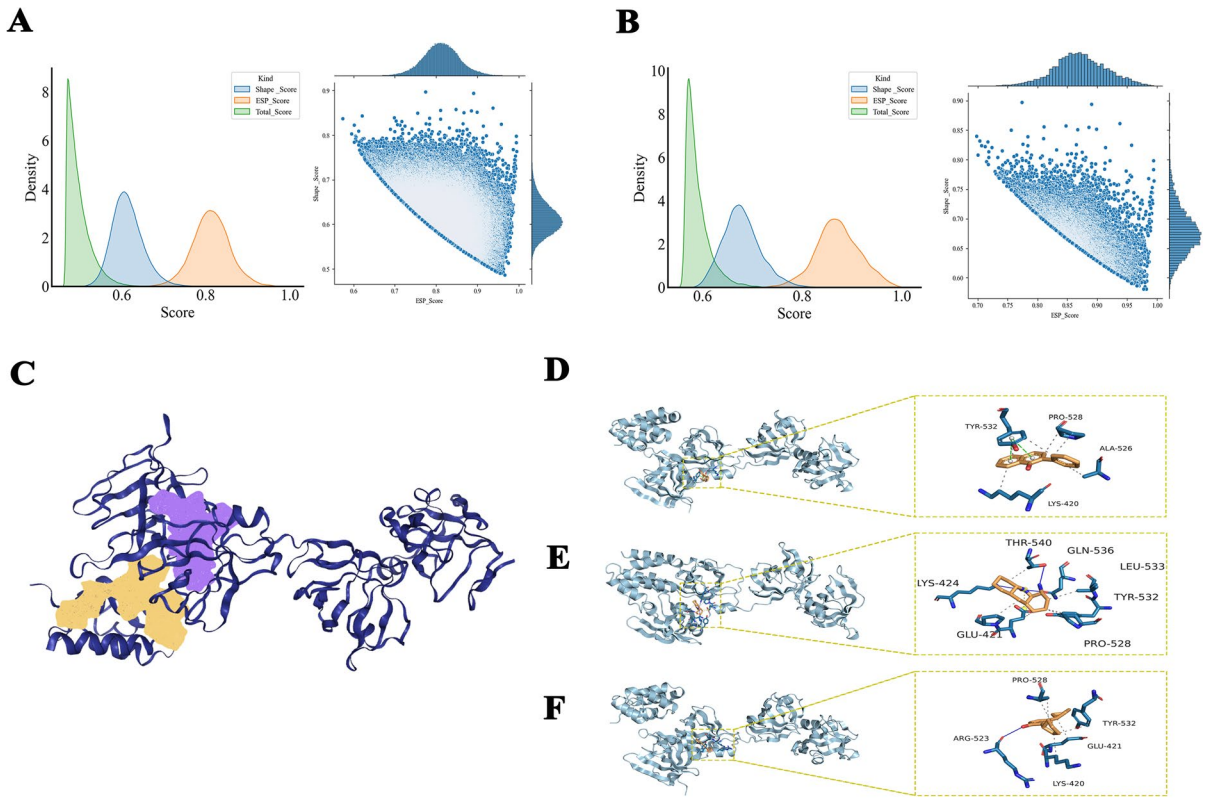

Fig. 11 Analysis of the results of combining IFI204 with molecule compounds. **A** The results of Lipinski rule screening (RDKit) from the database. **B** The top 5% of molecule compounds further screened by Espsim. **C** Schematic diagram of protein pocket prediction. **D-F** The binding mode of IFI204 to molecule compounds, respectively. The blue cartoon is the protein, the dark blue stick is the residue, and the ligand (molecule compounds) is the yellow stick

targets, providing a theoretical basis for subsequent drug development.

Discussion

Impairment of mitochondrial function and microglia pyroptosis caused by overactivated microglia is a crucial factor in traumatic brain injury (Robertson et al. 2007). However, there is limited knowledge regarding the brain factors that control this impairment and the underlying mechanisms. This study aims to explore how IFI204 contributes to the impairment of mitochondrial function and the pyroptosis of microglia, and elucidates its underlying molecular mechanisms. This work demonstrated that IFI204 in microglia and IFI204 expression was significantly increased following TBI. Eliminating IFI204 markedly enhances neurological impairments caused by TBI, which was found to have a positive correlation with reduced microglial activation, decreased pro-inflammatory responses, microglial pyroptosis, infarct sizes, and so on. Additionally, our investigation revealed that IFI204 can interact with SENP7, establishing a foundation for a clear physical connection between these two effectors. Following the genetic suppression of SENP7, the microglial pyroptosis influenced by STING and the associated mitochondrial dysfunction were mitigated, suggesting that STING signaling is essential for the occurrence of microglial pyroptosis.

In this research, we discovered 9 distinct cell types, such as astrocytes, endothelial cell, pericytes, neuron, microglia, T cells, B cells, SMCs and oligodendrocyte utilizing scRNA-seq data before and after TBI. Among various cell types, microglia and astrocytes represented the largest proportion of total cells after TBI. This finding aligns with previous observations that microglia and astrocytes constitute the main population of glial cells in mice affected by TBI (Todd et al. 2021). Microglia, the most abundant glial cells, exhibit significant activation and proliferation following TBI, which is crucial for the brain's response to injury (Ahmad et al. 2022). Microglia are natural immune cells that are quickly stimulated after brain injury, resulting in morphological and functional alterations and increased expression of surface markers. In contrast, astrocytes, known for their supportive function in maintaining homeostasis and protecting neurons, may undergo reactive astrogliosis after TBI as well as astrocyte morphology and Functional changes often lead to a reduction in either the overall population of astrocytes or a decrease in specific markers (Witcher 2018; Jayakumar 2014). Our results showed that an increase in microglia and a relative decrease in astrocytes after brain trauma, which is consistent with previous studies. Activated microglia can be categorized into various subpopulations based on their response to injury or disease. For instance, Ma et al. identified eight distinct subpopulations of microglia (three homeostatic clusters and five reactive clusters primarily appeared following ischemic stroke, referred to as Mic_M1L1, Mic_M1L2, Mic_np1, Mic_np2, and Mic_np3), including neurodegeneration-associated and interferon pathway-activated clusters, which highlight the diverse roles microglia can adopt in response to pathological conditions (Ma 2023). It has been reported that microglia are divided into two phenotypes, M1 and M2, and this classification is of great significance in understanding the function of microglia and regulating neuroinflammation (Yang 2023). Our results showed that sub-clustering analysis identified one homeostatic microglia and four non-steady-state microglia subpopulations based on marker genes namely axonogenesis, migration, interferon, and inflammatory microglia. We report, the identification of a novel microglia subpopulation that exhibits unique transcriptional profiles and functional characteristics distinct from the traditional M1 and M2 classifications. This discovery could improve our comprehension of the alterations in microglial phenotypes occurring during the initial stage of TBI.

The extensive alterations and specificity of gene expression during different periods effectively reflect the transcriptional features associated with the differentiation of microglia. Initially, microglia are activated within minutes of injury, as the injury evolves, microglia can further polarize into distinct phenotypes. The transition to an inflammatory state is marked by the production of pro-inflammatory cytokines and interferon signaling. Wu et al. highlighted that microglial activation leads to M1 polarization, which exacerbates neuroinflammation and neuronal dysfunction (Wu 2021). Emerging evidence demonstrates that genetic ablation of the type-1 interferon receptor confers neuroprotection in murine models of TBI, thereby underscoring the pivotal role of interferon signaling in perpetuating neuroinflammatory cascades associated with TBI

pathogenesis (Fritsch 2022). This transition is critical as it can influence the overall outcome of the injury, with M1 microglia contributing to further neuronal damage through excessive inflammatory responses. Our trajectory analysis suggested that the expression of genes Ccl3, Ccl4, lfi204, and Isg15 related to microglial IFN and inflammatory responses in the C1 subpopulation gradually increases during the progression of TBI. Consistently, as pseudotime progressed, genes related to microglial axonogenesis (Cldn5, Cldn11, Mal, Nkx6-2, Plp1, Pllp) and IFN microglia (lfitm3, Oasl2 and lfit1) expression was enhanced. Furthermore, genes enriched in the C3 pattern and closely related to microglial migration, including Atp1b2, Ptn, and Ptprz1, increased at the beginning of the trajectory and gradually decreased as the disease progressed. We have supplemented previous research reports and reported for the first time that microglia gradually transform from migrating cells into inflammatory, interferon and axonal microglia after TBI. In summary, inflammation, IFN and axonogenic microglia-related signaling pathways promote the progression of TBI.

Astrocytes, are crucial in reacting to brain injuries. Long et al. demonstrate that astrocyte-derived exosomes can inhibit neuroinflammation by modulating microglial phenotypes after traumatic brain injury (Long 2020). Therefore, it is very necessary to study astrocytes. Astrocytes exhibit a range of reactive states when responding to brain injury, which can be classified into at least two distinct reactivity profiles: reactivity 1 and reactivity 2. Research indicates that reactive astrocytes can adopt both neuroprotective and neurotoxic roles depending on the context of the injury (Jiwaji 2022;, Price et al. 2021). Chen et al. explored the mitochondrial oxidative phosphorylation protein levels in astrocytes, indicating that alterations in these pathways could be critical in understanding astrocytic responses to injury (Chen 2022). Such insights suggest that the metabolic state of astrocytes is a key factor in their functional classification post-injury. Moreover, the role of astrocytes in synaptic maintenance and plasticity is crucial in the context of brain trauma. Research by Hulshof et al. indicates that reactive astrocytes are involved in synapse loss during Alzheimer's disease, which could be extrapolated to other forms of brain injury (Hulshof et al. 2022). This synaptic involvement is further supported by studies indicating that astrocytes actively participate in synaptic remodeling and stabilization, particularly following traumatic events (Diaz et al. 2019;, Schiweck et al. 2018). Our results indicate that sub-clustering analysis identified several distinct astrocyte populations, including oxidative phosphorylation (OXPHOS)-related astrocytes (Chchd10, Cox5a, Cycs, and Nupr1), reactive astrocytes type 1 (Apoe and Clu), reactive astrocytes type 2 (Enpp2, Padi2, Plec, and Thbs4), and synaptic astrocytes (Dlx1 and Dlx2). Additionally, AST3 displayed a significant enrichment of neurogenesis and neuronal differentiation markers. These findings reveal novel subsets and diverse functions of astrocytes at 7 days post-injury (dpi) following TBI, which aligns with previous research. We further employed trajectory analysis, which demonstrated that synaptic astrocytes emerged at the beginning of the trajectory, while OXPHOS and reactive type 2 astrocytes gradually increased, and reactive type 1 astrocytes were observed at the end of the trajectory. GSEA revealed that the lipid metabolism signaling pathway was significantly enriched in reactive astrocytes, whereas synaptic astrocytes were predominantly enriched in cytoskeletal organization. These results suggest that oxidative stress and reactive astrocytes play a critical role in brain injury following TBI.

Data from single-cell RNA sequencing identified the upregulation of interferon-responsive genes as a key pathway in microglia 7 days after injury (Sen 2020). Recent studies indicate that after contusion TBI, neuronal stress results in heightened levels of STING expression in affected neurons. This activation triggers the release of type-1 interferon from neurons, leading to subsequent cytokine and chemokine release from microglia. STING expression has also been observed in postmortem human tissue during later stages of injury (Abdullah et al. 2018). Studies using IFN-β knock-out mice demonstrated a decrease in lesion size, protection against the loss of hippocampal neurons, and improved chronic behavioral deficits (Barrett 2020). Notably, these studies utilized a focal controlled cortical impact (CCI) injury model, revealing increased STING expression in the cortex following diffuse TBI, where neurons suffer injury (Greer et al. 2011)and mitochondrial dysfunction (Harris et al. 2001). Our Single-cell RNA sequencing dataset identified specific cell types responsible for producing interferons 7 days after injury. Our findings suggest that certain subpopulations of microglia

exhibit a strong response to IFN signals at this time, probably triggered by neurons and glia in reaction to cellular and mechanical injury following TBI.

The brain tissue and neurological function are particularly vulnerable to damage resulting from TBI (Ritzel 2019). Following a TBI, motor coordination deteriorates and muscular strength weakens. In this research, we investigated the impact of IFI204 cKOon neurological function in mice after TBI by evaluating their performance on the rotarod, mNSS scores, and grip force. Our findings provide the initial evidence that IFI204 knockout promotes neurological recovery by enhancing locomotor coordination and muscle strength. In addition, HE and Nissl staining revealed that IFI204 knockout significantly reduced neuronal damage following TBI. These results suggest that the depression of IFI204 mitigates TBI-induced cortical damage and improves behavioral deficits.

TBI often induces oxidative stress, which is strongly linked to the death of neurons (Wang 2022;, Kim et al. 2023). During periods of oxidative stress, an overproduction of ROS and MDA occurs (Sun et al. 2022). MDA, a key biomarker of ROS metabolism, is formed as a result of the breakdown of unsaturated lipids due to ROS. The concentration of MDA within cells may serve as an indicator of oxidative stress-induced cellular damage. Antioxidant mechanisms are capable of directly eliminating free radicals like ROS. Oxidative stress leads to a significant rise in ROS within cells, which impairs the mitochondrial membrane potential, harms the structural integrity of the mitochondrial membrane, damages mitochondrial DNA, and disrupts the electron transport chain, ultimately affecting mitochondrial function. Consequently, these oxidative stress effects can result in neuronal apoptosis, degeneration, and cell death (Apostolova et al. 2010). Our results demonstrate that IFI204 knockout decreases the levels of ROS and MDA induced by TBI by enhancing the antioxidant system. In addition, IFI204 knockout can reduce the mitochondrial membrane potential. Overall, these findings indicate that IFI204 knockout can protect microglia cells from oxidative stress-induced mitochondrial dysfunction after TBI, highlighting a promising and innovative therapeutic strategy.

Pyroptosis is initiated by inflammatory mechanisms across various cell types in diseases (Bian 2020).This process is activated by inflammasomes, which induce Caspase-1 to cleave GSDMD and release its N-terminal fragment (Ding 2016). The oligomerization of this fragment facilitates membrane pore formation, driving the extracellular release of inflammatory mediators (Chang 2020; Zhang 2019). This process holds particular significance in the realm of TBI, where the activation of microglial cells and the subsequent pyroptotic cell death contribute significantly to the neuroinflammatory response observed post-injury (Feng 2022). Emerging evidence suggests that the absence of Caspase-1 may alleviate neuroinflammatory processes in stroke, encephalomyelitis, TBI, and related neurological disorders. This therapeutic approach has been shown to promote neural repair mechanisms through the downregulation of key inflammasome components and pyroptotic mediators, including IL-1β, IL-18, and GSDMD, within the central nervous system (Ray et al. 2000;, Ross et al. 2007). Evidence indicates that direct inhibition or obstruction of GSDMD cleavage can significantly reduce cellular pyroptosis and enhance neurobehavioral outcomes, thereby aiding in the preservation of brain functionality (Yang 2018).Consequently, addressing NLRP3 inflammasome-mediated neuroinflammation and pyroptosis is vital for enhancing neurological function in mice affected by TBI. Previous research has shown that TBI in mice resulted in heightened expression of interferon type I-related genes (such as Ifnb1, Irf7, IFI204, Isg15). This elevation might play a role in the harmful neuroinflammatory reactions and neurological deficits seen in TBI models (Chunfa 2017). Our results showed that the increase in pyroptosis-associated proteins induced by TBI was diminished after the treatment with IFI204 knockout. These results indicate that IFI204 knockout can reduce the translocation of the N-terminal domain of GSDMD to the cell membrane by decreasing the activity of Caspase-1, inhibit the occurrence of pyroptosis, and decrease pro-inflammatory cytokines.

The cGAS-STING signaling pathway is essential in the modulation of diverse cellular processes (Shi 2023). cGAS catalyzes the synthesis of cyclic GMP-AMP (cGAMP) by combining ATP and GTP. This secondary messenger binds to the C-terminal ligand-binding domain (LBD) within STING dimers. Ligand engagement triggers STING conformational changes, facilitating TBK1 recruitment and subsequent phosphorylation of STING, TBK1, and IRF3. Activated IRF3 translocates to the nucleus to initiate IFNβ mRNA transcription and ISG expression. These

processes synergize with transcription factors such as NF-κB and STAT6, amplifying proinflammatory gene activation through cooperative transcriptional regulation (Wang 2018). Recent studies indicate that the STING-dependent signaling pathway can be activated and promote neuroinflammation, neuronal apoptosis, and neurological deficits through in mice with TBI (Shi 2023). Additional research indicates that STING signaling exerts dual regulatory functions in innate immunity. Beyond augmenting proinflammatory pathways and immune responses via TBK1-mediated activation of transcription factors, this molecular cascade concurrently activates multiple programmed cell death mechanisms. These encompass classical apoptotic pathways, necroptotic signaling cascades, pyroptotic inflammasome activation, and lysosome-dependent cellular demise (Tang et al. 2019). Following cerebral ischemia–reperfusion (I/R) injury, studies have demonstrated that STING interacts with NLRP3, facilitating pyroptosis in microglial cells (Li 2024). Furthermore, the STING signaling pathway, which is critical for type I interferon responses during antibacterial immune processes, is triggered by IFI204 (Storek et al. 2015). Recent studies involving mouse B16 melanoma cells and bone marrow-derived macrophages have further highlighted the necessity of IFI204 for STING activation (Chen 2019). Importantly, STING is predominantly found in neurons and microglia within the brain (Sen 2020). Therefore, it is plausible to suggest that IFI204 may promote microglial pyroptosis in TBI through activation of STING. Similarly, our

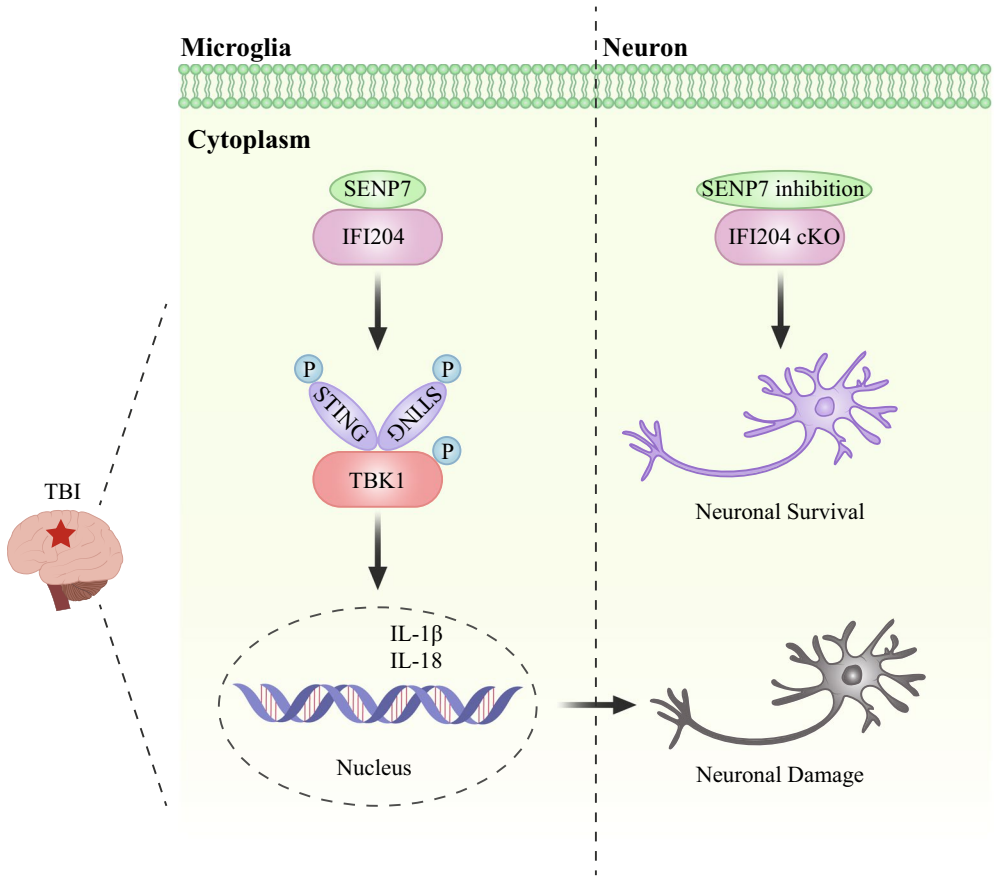

Fig. 12 Schematic diagram of IFI204 and its mechanism of regulating microglia-mediated TBI injury. IFI204 contributes to neurodegenerative deficits following TBI through the mediation of mitochondrial dysfunction and induction of microglial pyroptosis. Mechanistic analyses demonstrate that SENP7 interacts with IFI204, leading to deSUMOylation of IFI204. Activation of STING leads to mitochondrial dysfunction and microglial pyroptosis after TBI

study revealed that the STING-dependent signaling pathway was predominantly activated in microglia in mice subjected to TBI. IFI204 depression led to a loss of inducible phosphorylation of STING, moreover, the STING activator can significantly activate the STING signaling pathway inhibited by IFI204 knockout, which suggests that IFI204 is crucial for STING activation. Collectively, these results indicated that STING-dependent signaling pathway promotes microglia pyroptosis after TBI, IFI204 knockout can inhibit STING activation, reduce caspase-1 activity, decrease the formation of GSDMD-N, suppress cell pyroptosis.

SUMOylation's regulation of STING signaling in antiviral immunity has been well-documented (Cui 2017;, Hu 2016), however, the involvement of SUMOylation in STING-induced TBI is still unknown. The human SENP family comprises six isoforms (Liu 2023). Emerging evidence indicates that SENP7 plays a regulatory role in augmenting cGAS-mediated signaling pathways, thereby driving the proliferation of γδT lymphocytes with proinflammatory characteristics in inflammatory bowel disease (IBD) (Cui 2017;, Suhail 2019). Recent investigations have revealed that the binding between SENP3 and IFI204, thereby catalyzing IFI204 deSUMOylation, subsequently enhancing the activation of STING-dependent signaling pathways in murine models. This molecular mechanism promotes dendritic cell-mediated antitumor responses within the tumor-associated microenvironment (Hu 2021). By employing lentivirus to reduce SENP7 expression, we demonstrated an interaction between SENP7 and IFI204, which promotes the deSUMOylation of IFI204 and enhances the activation of STING signaling in microglial cells. Moreover, the findings from MD simulation and molecular docking studies demonstrated a robust and stable interaction between IFI204 and SENP7. Additionally, these results indicated a strong and lasting association of IFI204 with molecular compounds, which provides a theoretical basis for future drug development. For a visual representation, please refer to Fig. 12, which presents a schematic diagram elucidating the findings.

While the current investigation confirms the involvement of IFI204 in cerebral injury pathogenesis, several constraints remain unresolved. Subsequent investigations should prioritize elucidating prolonged neurological and mitochondrial function recovery using in vitro primary microglial cultures and murine brain injury models. Furthermore, future research could further explore how IFI204 may influence overall inflammatory outcomes by modulating the interaction between microglia and astrocytes, thereby avoiding the limitations of focusing solely on a single cell type.

Conclusion

Our research shows that IFI204 knockout improves neurological function in mice with cerebral TBI by inhibiting microglial mitochondrial dysfunction and pyroptosis. Specifically, we observed that the interaction between SENP7 and IFI204 results in the deSUMOylation of IFI204, which in turn activates the STING signaling pathway after TBI. This activation results in motor function deficits, mitochondrial dysfunction, and cell pyroptosis. Findings from this study demonstrate that IFI204 knockout emerges as a potential therapeutic strategy for the treatment of TBI.

Acknowledgements Not applicable

Author contributions LF contributed the design of the work, GT, CJH, LYX and WSG contributed to the majority of experiments, data analysis and manuscript writing. LCJ, ZXY, LPQ performed the data analysis and animal experiments. ZMW reviewed the manuscript critically. The final manuscript was reviewed and approved by all authors.

Funding This work was supported by Joint Funds for the innovation of science and Technology, Fujian province (Grant number:2023Y9277), Natural Science Foundation of Fujian Province (No. 2022 J05072).

Data availability No datasets were generated or analysed during the current study.

Declarations

Ethical approval The methods used in the experiment complied with the rules set forth by the National Institutes of Health (NIH Publications NO. 80–23, revised in 1996). All the procedures for experimentation received approval from the Institutional Animal Care and Use Committee (IACUC) at Fujian Provincial Hospital in Fujian, China.

Competing interests The authors declare no competing interests.

References

Abdullah A, Zhang M, Frugier T, Bedoui S, Taylor JM, Crack PJ. STING-mediated type-I interferons contribute to the neuroinflammatory process and detrimental effects following traumatic brain injury. J Neuroinflammation. 2018;15:323. https://doi.org/10.1186/s12974-018-1354-7.

Ahmad R, Khan A, Rehman IU, Lee HJ, Khan I, Kim MO. Lupeol treatment attenuates activation of glial cells and oxidative-stress-mediated neuropathology in mouse model of traumatic brain injury. Int J Mol Sci. 2022;23:6086. https://doi.org/10.3390/ijms23116086.

Apostolova N, Gomez-Sucerquia LJ, Moran A, Alvarez A, Blas-Garcia A, Esplugues JV. Enhanced oxidative stress and increased mitochondrial mass during efavirenz-induced apoptosis in human hepatic cells. Br J Pharmacol. 2010;160:2069–84. https://doi.org/10.1111/j.1476-5381.2010.00866.x.

Barrett JP, et al. Interferon-β Plays a Detrimental Role in Experimental Traumatic Brain Injury by Enhancing Neuroinflammation That Drives Chronic Neurodegeneration. J Neurosci. 2020;40:2357–70. https://doi.org/10.1523/jneurosci.2516-19.2020.

Bawa-Khalfe T, et al. Differential expression of SUMO-specific protease 7 variants regulates epithelial-mesenchymal transition. Proc Natl Acad Sci U S A. 2012;109:17466–71. https://doi.org/10.1073/pnas.1209378109.

Bian Y, et al. Kanglexin, a novel anthraquinone compound, protects against myocardial ischemic injury in mice by suppressing NLRP3 and pyroptosis. Acta Pharmacol Sin. 2020;41:319–26. https://doi.org/10.1038/s41401-019-0307-8.

Cao Y, Huang C, Zhao X, Yu J. Regulation of SUMOylation on RNA metabolism in cancers. Front Mol Biosci. 2023;10:1137215. https://doi.org/10.3389/fmolb.2023.1137215.

Chang Y, et al. NLRP3 inflammasome-mediated microglial pyroptosis is critically involved in the development of post-cardiac arrest brain injury. J Neuroinflammation. 2020;17:219. https://doi.org/10.1186/s12974-020-01879-1.

Chen W, et al. DNA Sensor IFI204 Contributes to Host Defense Against Staphylococcus aureus Infection in Mice. Front Immunol. 2019;10:474. https://doi.org/10.3389/fimmu.2019.00474.

Chen C, et al. Astrocytic Changes in Mitochondrial Oxidative Phosphorylation Protein Levels in Parkinson's Disease. Mov Disord. 2022;37:302–14. https://doi.org/10.1002/mds.28849.

Chen X, Lao Y, Yi J, Yang J, He S, Chen Y. SENP3 in monocytes/macrophages up-regulates tissue factor and mediates lipopolysaccharide-induced acute lung injury by enhancing JNK phosphorylation. J Cell Mol Med. 2020;24:5454–62. https://doi.org/10.1111/jcmm.15199.

Choubey D, et al. Interferon-inducible p200-family proteins as novel sensors of cytoplasmic DNA: role in inflammation and autoimmunity. J Interferon Cytokine Res. 2010;30:371–80. https://doi.org/10.1089/jir.2009.0096.

Chunfa L, et al. The Central Role of IFI204 in IFN-β Release and Autophagy Activation during Mycobacterium bovis Infection. Front Cell Infect Microbiol. 2017;7:169. https://doi.org/10.3389/fcimb.2017.00169.

Cui Y, et al. SENP7 Potentiates cGAS Activation by Relieving SUMO-Mediated Inhibition of Cytosolic DNA Sensing. PLoS Pathog. 2017;13:e1006156. https://doi.org/10.1371/journal.ppat.1006156.

Dewan MC, et al. Estimating the global incidence of traumatic brain injury. J Neurosurg. 2018;130:1080–97. https://doi.org/10.3171/2017.10.Jns17352.

Diaz A, Merino P, Manrique LG, Cheng L, Yepes M. Urokinase-type plasminogen activator (uPA) protects the tripartite synapse in the ischemic brain via ezrin-mediated formation of peripheral astrocytic processes. J Cereb Blood Flow Metab. 2019;39:2157–71. https://doi.org/10.1177/0271678x18783653.

Ding J, et al. Pore-forming activity and structural autoinhibition of the gasdermin family. Nature. 2016;535:111–6. https://doi.org/10.1038/nature18590.

Downey CM, Aghaei M, Schwendener RA, Jirik FR. DMXAA causes tumor site-specific vascular disruption in murine non-small cell lung cancer, and like the endogenous non-canonical cyclic dinucleotide STING agonist, 2'3'-cGAMP, induces M2 macrophage repolarization. PLoS ONE. 2014;9:e99988. https://doi.org/10.1371/journal.pone.0099988.

Du C, et al. The Function of SUMOylation and Its critical roles in cardiovascular diseases and potential clinical implications. Int J Mol Sci. 2021;22:10618. https://doi.org/10.3390/ijms221910618.

Feng Z, et al. Mesenchymal stem cells protect against TBI-induced pyroptosis in vivo and in vitro through TSG-6. Cell Commun Signal. 2022;20:125. https://doi.org/10.1186/s12964-022-00931-2.

Fritsch LE, et al. Type I Interferon Response Is Mediated by NLRX1-cGAS-STING Signaling in Brain Injury. Front Mol Neurosci. 2022;15:852243. https://doi.org/10.3389/fnmol.2022.852243.

Fukuoka M, et al. Supplemental treatment for Huntington's disease with miR-132 that is deficient in Huntington's disease brain. Mol Ther Nucleic Acids. 2018;11:79–90. https://doi.org/10.1016/j.omtn.2018.01.007.

Gaidt MM, et al. The DNA inflammasome in human myeloid cells is initiated by a STING-cell death program upstream of NLRP3. Cell. 2017;171:1110-1124.e1118. https://doi.org/10.1016/j.cell.2017.09.039.

Gao G, et al. Glutaminase C regulates microglial activation and pro-inflammatory exosome release: Relevance to the pathogenesis of Alzheimer's disease. Front Cell Neurosci. 2019;13:264. https://doi.org/10.3389/fncel.2019.00264.

Garvin AJ, et al. The deSUMOylase SENP7 promotes chromatin relaxation for homologous recombination DNA repair. EMBO Rep. 2013;14:975–83. https://doi.org/10.1038/embor.2013.141.

Greer JE, McGinn MJ, Povlishock JT. Diffuse traumatic axonal injury in the mouse induces atrophy, c-Jun activation, and axonal outgrowth in the axotomized neuronal population. J Neurosci. 2011;31:5089–105. https://doi.org/10.1523/jneurosci.5103-10.2011.

Guo T, et al. Neuropilin-1 promotes mitochondrial structural repair and functional recovery in rats with cerebral ischemia. J Transl Med. 2023;21:297. https://doi.org/10.1186/s12967-023-04125-3.

Harris LK, Black RT, Golden KM, Reeves TM, Povlishock JT, Phillips LL. Traumatic brain injury-induced changes in gene expression and functional activity of mitochondrial cytochrome C oxidase. J Neurotrauma. 2001;18:993–1009. https://doi.org/10.1089/08977150152693692.

Heiman M, et al. A translational profiling approach for the molecular characterization of CNS cell types. Cell. 2008;135:738–48. https://doi.org/10.1016/j.cell.2008.10.028.

Hu MM, et al. Sumoylation Promotes the Stability of the DNA Sensor cGAS and the Adaptor STING to Regulate the Kinetics of Response to DNA Virus. Immunity. 2016;45:555–69. https://doi.org/10.1016/j.immuni.2016.08.014.

Hu Z, et al. SENP3 senses oxidative stress to facilitate STING-dependent dendritic cell antitumor function. Mol Cell. 2021;81:940-952.e945. https://doi.org/10.1016/j.molcel.2020.12.024.

Hulshof LA, van Nuijs D, Hol EM, Middeldorp J. The role of astrocytes in synapse loss in alzheimer's disease: A systematic review. Front Cell Neurosci. 2022;16:899251. https://doi.org/10.3389/fncel.2022.899251.

Hwang JT, Lee A, Kho C. Ubiquitin and Ubiquitin-like proteins in cancer, neurodegenerative disorders, and heart diseases. Int J Mol Sci. 2022;23:50583. https://doi.org/10.3390/ijms23095053.

Irwin JJ, et al. ZINC20-A free ultralarge-scale chemical database for ligand discovery. J Chem Inf Model. 2020;60:6065–73. https://doi.org/10.1021/acs.jcim.0c00675.

Jayakumar AR, et al. Activation of NF-κB mediates astrocyte swelling and brain edema in traumatic brain injury. J Neurotrauma. 2014;31:1249–57. https://doi.org/10.1089/neu.2013.3169.

Jiwaji Z, et al. Reactive astrocytes acquire neuroprotective as well as deleterious signatures in response to Tau and Aß pathology. Nat Commun. 2022;13:135. https://doi.org/10.1038/s41467-021-27702-w.

Juárez-Rebollar D, Rios C, Nava-Ruíz C, Méndez-Armenta M. Metallothionein in brain disorders. Oxid Med Cell Longev. 2017;2017:5828056. https://doi.org/10.1155/2017/5828056.

Jumper J, et al. Highly accurate protein structure prediction with AlphaFold. Nature. 2021;596:583–9. https://doi.org/10.1038/s41586-021-03819-2.

Katrin S-S, et al. ProteinsPlus: interactive analysis of protein–ligand binding interfaces. Nucleic Acids Res. 2020. https://doi.org/10.1093/nar/gkaa235.

Kerr N, Dietrich DW, Bramlett HM, Raval AP. Sexually dimorphic microglia and ischemic stroke. CNS Neurosci Ther. 2019;25:1308–17. https://doi.org/10.1111/cns.13267.

Khellaf A, Khan DZ, Helmy A. Recent advances in traumatic brain injury. J Neurol. 2019;266:2878–89. https://doi.org/10.1007/s00415-019-09541-4.

Kim K, Hong HL, Kim GM, Leem J, Kwon HH. Eupatilin ameliorates lipopolysaccharide-induced acute kidney injury by inhibiting inflammation, oxidative stress, and apoptosis in mice. Curr Issues Mol Biol. 2023;45:7027–42. https://doi.org/10.3390/cimb45090444.

Lao Y, et al. DeSUMOylation of MKK7 kinase by the SUMO2/3 protease SENP3 potentiates lipopolysaccharide-induced inflammatory signaling in macrophages. J Biol Chem. 2018;293:3965–80. https://doi.org/10.1074/jbc.M117.816769.

Li X, et al. Mib2 deficiency inhibits microglial activation and alleviates ischemia-induced brain injury. Aging Dis. 2020;11:523–35. https://doi.org/10.14336/ad.2019.0807.

Li W, et al. STING mediates microglial pyroptosis via interaction with NLRP3 in cerebral ischaemic stroke. Stroke Vasc Neurol. 2024;9:153–64. https://doi.org/10.1136/svn-2023-002320.

Li X, Jiao F, Hong J, Yang F, Wang L, Gong Z. SENP7 knockdown inhibited pyroptosis and NF-κB/NLRP3 inflammasome pathway activation in Raw 264.7 cells. Sci Rep. 2020;10:16265. https://doi.org/10.1038/s41598-020-73400-w.

Lin Q, et al. K6-linked SUMOylation of BAF regulates nuclear integrity and DNA replication in mammalian cells. Proc Natl Acad Sci U S A. 2020;117:10378–87. https://doi.org/10.1073/pnas.1912984117.

Liu C, et al. MyoD-dependent induction during myoblast differentiation of p204, a protein also inducible by interferon. Mol Cell Biol. 2000;20:7024–36. https://doi.org/10.1128/mcb.20.18.7024-7036.2000.

Liu A, et al. Ginsenoside Rb1 administration attenuates focal cerebral ischemic reperfusion injury through inhibition of HMGB1 and inflammation signals. Exp Ther Med. 2018;16:3020–6. https://doi.org/10.3892/etm.2018.6523.

Liu Y, et al. Mitochondrial SENP2 regulates the assembly of SDH complex under metabolic stress. Cell Rep. 2023;42:112041. https://doi.org/10.1016/j.celrep.2023.112041.

Long X, et al. Astrocyte-derived exosomes enriched with miR-873a-5p inhibit neuroinflammation via microglia phenotype modulation after traumatic brain injury. J Neuroinflammation. 2020;17:89. https://doi.org/10.1186/s12974-020-01761-0.

Luo W, et al. Critical role of cytosolic DNA and its sensing adaptor STING in aortic degeneration, dissection, and rupture. Circulation. 2020;141:42–66. https://doi.org/10.1161/circulationaha.119.041460.

Ma H, et al. Microglia exhibit distinct heterogeneity rather than M1/M2 polarization within the early stage of acute ischemic stroke. Aging Dis. 2023;14:2284–302. https://doi.org/10.14336/ad.2023.0505.

Mondini M, Costa S, Sponza S, Gugliesi F, Gariglio M, Landolfo S. The interferon-inducible HIN-200 gene family in apoptosis and inflammation: implication for autoimmunity. Autoimmunity. 2010;43:226–31. https://doi.org/10.3109/08916930903510922.

Persano L, et al. Interferon-alpha counteracts the angiogenic switch and reduces tumor cell proliferation in a spontaneous model of prostatic cancer. Carcinogenesis. 2009;30:851–60. https://doi.org/10.1093/carcin/bgp052.

Price BR, Johnson LA, Norris CM. Reactive astrocytes: The nexus of pathological and clinical hallmarks of Alzheimer's disease. Ageing Res Rev. 2021;68:101335. https://doi.org/10.1016/j.arr.2021.101335.

Qiu X, et al. Reversed graph embedding resolves complex single-cell trajectories. Nat Methods. 2017;14:979–82. https://doi.org/10.1038/nmeth.4402.

Ray AM, Owen DE, Evans ML, Davis JB, Benham CD. Caspase inhibitors are functionally neuroprotective against oxygen glucose deprivation induced CA1 death in rat organotypic hippocampal slices. Brain Res. 2000;867:62–9. https://doi.org/10.1016/s0006-8993(00)02230-7.

Ritzel RM, et al. Old age increases microglial senescence, exacerbates secondary neuroinflammation, and worsens neurological outcomes after acute traumatic brain injury in mice. Neurobiol Aging. 2019;77:194–206. https://doi.org/10.1016/j.neurobiolaging.2019.02.010.

Robertson CL, Saraswati M, Fiskum G. Mitochondrial dysfunction early after traumatic brain injury in immature rats. J Neurochem. 2007;101:1248–57. https://doi.org/10.1111/j.1471-4159.2007.04489.x.

Ross J, Brough D, Gibson RM, Loddick SA, Rothwell NJ. A selective, non-peptide caspase-1 inhibitor, VRT-018858, markedly reduces brain damage induced by transient ischemia in the rat. Neuropharmacology. 2007;53:638–42. https://doi.org/10.1016/j.neuropharm.2007.07.015.

Sanders OD. Virus-like cytosolic and cell-free oxidatively damaged nucleic acids likely drive inflammation, synapse degeneration, and neuron death in Alzheimer's disease. J Alzheimers Dis Rep. 2023;7:1–19. https://doi.org/10.3233/adr-220047.

Sanz E, Yang L, Su T, Morris DR, McKnight GS, Amieux PS. Cell-type-specific isolation of ribosome-associated mRNA from complex tissues. Proc Natl Acad Sci U S A. 2009;106:13939–44. https://doi.org/10.1073/pnas.0907143106.

Schiweck J, Eickholt BJ, Murk K. Important shapeshifter: Mechanisms allowing astrocytes to respond to the changing nervous system during development. Injury Dis Front Cell Neurosci. 2018;12:261. https://doi.org/10.3389/fncel.2018.00261.

Sen T, et al. Aberrant ER stress induced neuronal-IFNβ elicits white matter injury due to microglial activation and T-Cell infiltration after TBI. J Neurosci. 2020;40:424–46. https://doi.org/10.1523/jneurosci.0718-19.2019.

Shen Q, et al. SiBaoChongCao exhibited anti-fatigue activities and ameliorated cancer cachexia in mice. RSC Adv. 2019;9:17440–56. https://doi.org/10.1039/c9ra00718k.

Shi G, et al. Inhibition of neutrophil extracellular trap formation ameliorates neuroinflammation and neuronal apoptosis via STING-dependent IRE1α/ASK1/JNK signaling pathway in mice with traumatic brain injury. J Neuroinflammation. 2023;20:222. https://doi.org/10.1186/s12974-023-02903-w.

Song S, et al. Microglial-oligodendrocyte interactions in myelination and neurological function recovery after traumatic brain injury. J Neuroinflammation. 2022;19:246. https://doi.org/10.1186/s12974-022-02608-6.

Storek KM, Gertsvolf NA, Ohlson MB, Monack DM. cGAS and Ifi204 cooperate to produce type I IFNs in response to Francisella infection. J Immunol. 2015;194:3236–45. https://doi.org/10.4049/jimmunol.1402764.

Su ZD, et al. Melatonin alleviates lipopolysaccharide-induced myocardial injury by inhibiting inflammation and pyroptosis in cardiomyocytes. Ann Transl Med. 2021;9:413. https://doi.org/10.21037/atm-20-8196.

Subramanian A, et al. Gene set enrichment analysis: a knowledge-based approach for interpreting genome-wide expression profiles. Proc Natl Acad Sci U S A. 2005;102:15545–50. https://doi.org/10.1073/pnas.0506580102.

Suhail A, et al. DeSUMOylase SENP7-Mediated Epithelial Signaling Triggers Intestinal Inflammation via Expansion of Gamma-Delta T Cells. Cell Rep. 2019;29:3522-3538.e3527. https://doi.org/10.1016/j.celrep.2019.11.028.

Sun KL, Gao M, Wang YZ, Li XR, Wang P, Wang B. Antioxidant peptides from protein hydrolysate of marine red algae eucheuma cottonii: Preparation, identification, and cytoprotective mechanisms on H(2)O(2) oxidative damaged HUVECs. Front Microbiol. 2022;13:791248. https://doi.org/10.3389/fmicb.2022.791248.

Tang D, Kang R, Berghe TV, Vandenabeele P, Kroemer G. The molecular machinery of regulated cell death. Cell Res. 2019;29:347–64. https://doi.org/10.1038/s41422-019-0164-5.

Thomas AH, Robert BN. Merck molecular force field. IV. conformational energies and geometries for MMFF94. J Comput Chem. 1996;17(5–6):587–615. https://doi.org/10.1002/(sici)1096-987x(199604)17:5/6<587::aid-jcc4>3.0.co;2-q.

Todd BP, Chimenti MS, Luo Z, Ferguson PJ, Bassuk AG, Newell EA. Traumatic brain injury results in unique microglial and astrocyte transcriptomes enriched for type I interferon response. J Neuroinflammation. 2021;18:151. https://doi.org/10.1186/s12974-021-02197-w.

UPJNAR Consortium (2021). UniProt: the universal protein knowledgebase in 2021. Nucleic Acids Res 49:480-489. https://doi.org/10.1093/nar/gkaa1100

Van Der Spoel D, Lindahl E, Hess B, Groenhof G, Mark AE, Berendsen HJ. GROMACS: fast, flexible, and free. J Comput Chem. 2005;26:1701–18. https://doi.org/10.1002/jcc.20291.

Wang PH, et al. A novel transcript isoform of STING that sequesters cGAMP and dominantly inhibits innate nucleic acid sensing. Nucleic Acids Res. 2018;46:4054–71. https://doi.org/10.1093/nar/gky186.

Wang JP, et al. Research progress on the inflammatory effects of long non-coding RNA in traumatic brain injury. Front

Mol Neurosci. 2022;15:835012. https://doi.org/10.3389/fnmol.2022.835012.

Wang Y, Yue X, Kiesewetter DO, Niu G, Teng G, Chen X. PET imaging of neuroinflammation in a rat traumatic brain injury model with radiolabeled TSPO ligand DPA-714. Eur J Nucl Med Mol Imaging. 2014;41:1440–9. https://doi.org/10.1007/s00259-014-2727-5.

Witcher KG, et al. Traumatic brain injury-induced neuronal damage in the somatosensory cortex causes formation of rod-shaped microglia that promote astrogliosis and persistent neuroinflammation. Glia. 2018;66:2719–36. https://doi.org/10.1002/glia.23523.

Witcher KG, et al. Traumatic brain injury causes chronic cortical inflammation and neuronal dysfunction mediated by microglia. J Neurosci. 2021;41:1597–616. https://doi.org/10.1523/jneurosci.2469-20.2020.

Wu H, et al. Mer regulates microglial/macrophage M1/M2 polarization and alleviates neuroinflammation following traumatic brain injury. J Neuroinflammation. 2021;18:2. https://doi.org/10.1186/s12974-020-02041-7.

Xia W, et al. Damaged brain accelerates bone healing by releasing small extracellular vesicles that target osteoprogenitors. Nat Commun. 2021;12:6043. https://doi.org/10.1038/s41467-021-26302-y.

Xu P, et al. Microglial TREM-1 receptor mediates neuroinflammatory injury via interaction with SYK in experimental ischemic stroke. Cell Death Dis. 2019;10:555. https://doi.org/10.1038/s41419-019-1777-9.

Xu H, et al. Brain-specific loss of Abcg1 disturbs cholesterol metabolism and aggravates pyroptosis and neurological deficits after traumatic brain injury. Brain Pathol. 2023;33:e13126. https://doi.org/10.1111/bpa.13126.

Yamaguchi H, Hiroi M, Ohmori Y. Silencing of the interferon-inducible gene Ifi204/p204 induces resistance to interferon-γ-mediated cell growth arrest of tumor cells. Cytokine. 2019;118:80–92. https://doi.org/10.1016/j.cyto.2018.06.029.

Yang J, et al. Mechanism of gasdermin D recognition by inflammatory caspases and their inhibition by a gasdermin D-derived peptide inhibitor. Proc Natl Acad Sci U S A. 2018;115:6792–7. https://doi.org/10.1073/pnas.1800562115.

Yang Y, et al. Sestrin2 provides cerebral protection through activation of Nrf2 signaling in microglia following subarachnoid hemorrhage. Front Immunol. 2023;14:1089576. https://doi.org/10.3389/fimmu.2023.1089576.

Yu G, Wang LG, Han Y, He QY. clusterProfiler: an R package for comparing biological themes among gene clusters. OMICS. 2012;16:284–7. https://doi.org/10.1089/omi.2011.0118.

Zhang D, et al. Gasdermin D serves as a key executioner of pyroptosis in experimental cerebral ischemia and reperfusion model both in vivo and in vitro. J Neurosci Res. 2019;97:645–60. https://doi.org/10.1002/jnr.24385.

Zhou Z, et al. Nuclear Nrf2 activity in laryngeal carcinoma is regulated by SENP3 after cisplatin-induced reactive oxygen species stress. J Cancer. 2019;10:3427–34. https://doi.org/10.7150/jca.30318.

Zhou J, Ventura CJ, Fang RH, Zhang L. Nanodelivery of STING agonists against cancer and infectious diseases. Mol Aspects Med. 2022;83:101007. https://doi.org/10.1016/j.mam.2021.101007.

Zhu HT, et al. Curcumin attenuates acute inflammatory injury by inhibiting the TLR4/MyD88/NF-κB signaling pathway in experimental traumatic brain injury. J Neuroinflammation. 2014;11:59. https://doi.org/10.1186/1742-2094-11-59.